

Facilitating megacity electricity decarbonization via grid-interactive demand-side resource management

Downloaded from: https://research.chalmers.se, 2026-11-03 03:00 UTC

Citation for the original published paper (version of record):
Li, K., Tao, S., Xiong, Z. et al (2026). Facilitating megacity electricity decarbonization via grid-interactive demand-side resource
management. Nature Communications, 17(1). http://dx.doi.org/10.1038/s41467-026-76799-4

N.B. When citing this work, cite the original published paper.

research.chalmers.se offers the possibility of retrieving research publications produced at Chalmers University of Technology. It covers all kind of research output: articles, dissertations, conference papers, reports etc. since 2004. research.chalmers.se is administrated and maintained by Chalmers Library

(article starts on next page)

nature communications

Article

https://doi.org/10.1038/s41467-026-76799-4

Facilitating megacity electricity decarbonization via grid-interactive demand-side resource management

Received: 12 January 2026

Accepted: 4 August 2026

Published online: 17 August 2026

Check for updates

Kaisan Li[1], Shengyu Tao[1,2], Zuxun Xiong[3], Ruojun Ren[1], Yuhang Zhang[1], Rui Miao[1], He Qi[4,5], Borong Lin[6], Jian Kang[7], Yi Jiang[1,6] & Yi Zhang[1]

City power systems face intensified mismatches between generation and dynamic demand under rising zero-carbon energy penetration levels. Although demand-side resource management offers mismatch mitigation potential by regulating load patterns, its city-level capability remains unclear. This study develops a community-to-grid framework to assess how demand-side resources could mitigate generation-demand mismatches at the megacity scale. A case study is performed in Shenzhen, China, covering 4,549 community units with energy profiles and rooftop photovoltaics of 479,259 buildings, and travel-charge profiles of 1,080,000 private plug-in electric vehicles. Under an assumed 80% zero-carbon electricity penetration level, the proposed framework could reduce weekly power supply deficits by 54.5%, or 266.2 gigawatt-hours, corresponding to an estimated reduction of 83.6 kilotonnes of carbon dioxide. Different governing paradigms may affect grid infrastructure upgrade paths: prioritizing administrative equity supports temporally consistent planning, whereas prioritizing mismatch-mitigation efficiency promotes spatially clustered retrofitting. This study may inform city-specific demand-side resource excavation under national electricity decarbonization planning.

China's macro policies for electricity decarbonization[1,2] are accelerating the phase-down of fossil-based generation and the deployment of zero-carbon electricity, primarily wind, solar, and nuclear[3,4]. As the primary administrative entity for this policy implementation at meso-scale, cities increasingly find themselves at the interface between planned zero-carbon deployment on the generation side and dynamic loads on the demand side. The resulting generation-demand mismatch[5] manifests as curtailment (excess generation) and shortage (insufficient generation), with the latter often necessitating fossil-based backup generation such as gas power[5,6] and thus yielding unplanned carbon emissions that impair the realized benefits of electricity decarbonization. Demand-side resource management (DSRM), which coordinates distributed assets such as rooftop photovoltaic (RPV), battery energy storage systems (BESSs), electric vehicles (EVs) and smart appliances[7,8] to reshape load patterns, offers an effective pathway for mitigating this mismatch. To translate national decarbonization targets into actionable community-level operations, cities therefore need a systematic understanding of both the achievable potential of DSRM and the implementation pathways required to progressively activate demand-side resources across diverse urban communities.

Research on electricity decarbonization exhibits distinct focuses across spatial scales. Macro-scale studies provide broad insights into renewable integration and demand-side resource deployment across

[1]Tsinghua Shenzhen International Graduate School, Tsinghua University, Shenzhen 518055, China. [2]Department of Electrical Engineering, Chalmers University of Technology, Gothenburg 41296, Sweden. [3]Department of Engineering Science, University of Oxford, Oxford OX1 3PJ, UK. [4]China Construction Eighth Engineering Division Corp. Ltd, Shanghai 200112, China. [5]State Key Laboratory of Green Building, Xi'an 710055, China. [6]Department of Building Science, School of Architecture, Tsinghua University, Beijing 100084, China. [7]Bartlett Faculty of Built Environment, University College London, London WC1E 6BT, UK. e-mail: zy1214@sz.tsinghua.edu.cn

countries, provinces and cities. Global power-system analyses show that wind-solar variability can intensify hourly generation-demand mismatches, requiring flexibility measures such as demand response (DR) and storage to control system costs[3]. Grid-coordination studies further show that expanded transmission and coordinated planning can reduce renewable curtailment, capacity overbuilding, and decarbonization costs[9,10]. China-focused studies quantify the large renewable, storage, flexible-generation, and transmission investments needed for carbon-neutral electricity supply[11], and reveal heterogeneous cost and emission effects of provincial BESS siting strategies[12]. Demand-side studies show household-level solar-battery economic and resilience benefits across the United States[13], while sector-electrification research highlights the need for flexible load design to avoid shifting emissions and security burdens to power grids[14]. City-comparative rooftop studies reveal strong spatial and building-type heterogeneity in urban rooftop production and deployable RPV potential[15,16]. However, these assessments rely mainly on highly aggregated and coarse-grained data, leaving unclear how heterogeneous RPV, BESSs, EVs, and building loads can be jointly scheduled within urban communities to mitigate city-level generation-demand mismatches under operational constraints.

Meso-scale studies have advanced city-level modeling of single demand-side resource. Real-world mobility and charging data have been used to quantify megacity-scale vehicle-to-grid (V2G) performance of private plug-in electric vehicles (P-PEVs), showing their substantial potential of city load shifting[17]. City-scale solar studies evaluate RPV, photovoltaic-thermal, and solar thermal potential under dense urban morphology and shading, but mainly address generation potential rather than coordinated DSRM operations[18]. Other studies quantify heating, ventilation and air conditioning flexibility across China's city clusters under climate diversity[19], or optimize BESS siting and sizing for urban energy resilience under extreme events[20]. In parallel, building-scale carbon attribution studies reveal strong spatial heterogeneity in operational emissions and propose urban decarbonization pathways, yet focus on carbon accounting and retrofit strategies rather than operational dispatch[21,22]. Therefore, existing meso-scale work remains largely single-resource or carbon-pathway oriented, leaving multi-resource DSRM potential for city-level mismatch mitigation insufficiently discussed.

Micro-scale studies provide detailed operational insights for neighborhoods, district-level integrated energy systems, and multi-microgrids. Neighborhood-scale demand-supply optimization shows that combining local PV, BESSs, and grid exchange can reduce building-related emissions with moderate cost increases[23]. District-level energy-hub dispatch studies incorporate carbon trading, privacy protection, and DR to improve low-carbon economic operation[24]. Multi-microgrid studies further show that peer-to-peer trading among heterogeneous building communities with EVs can improve self-consumption, autonomy, and economic performance[25]. However, their small-system perspectives do not directly support municipal assessment of city-wide, multi-resource DSRM potential.

Overall, existing studies have left insufficiently connected national decarbonization planning of generation mix, city-level generation-demand mismatch mitigation, and community-scale multi-resource DSRM operations within a unified framework, which impedes cities' downward translation of national policies into actionable local solutions. A summary table of existing studies is provided in Supplementary Tables 27–29.

In this study, a community-to-grid (C2G) framework is developed for fine-grained DSRM potential analysis at the city level. The framework uses community unit (CU), a functional living neighborhood aligned with urban transportation networks[26], as the basic scheduling unit. Each CU contains tens to hundreds of buildings, thousands of P-PEV visits, and 20,000 m^2 RPV area on average, which mitigates P-PEV positioning uncertainty while enabling the integration of user-centric P-PEV travel-charge predictions[17] into community-level scheduling. The framework is evaluated in Shenzhen, China, by decoupling the city into 4549 CUs and integrating hourly energy profiles of 479,259 non-industrial buildings, travel-charge patterns of 1.08 million P-PEVs, and up to 95.6 km^2 of available RPV area. Three zero-carbon penetration scenarios, ZC 30, ZC 50 and ZC 80, are designed to represent different stages of city decarbonization. Results show that scheduling Shenzhen's demand-side resources reduces amount of curtailment (AOC) by 95.5–231.1 GWh (47.3–65.7% of business-as-usual curtailments) and amount of shortage (AOS) by 57.4–266.2 GWh (39.5–54.5% of business-as-usual shortages), avoiding 21.1–83.6 kt CO_2 emissions. Implications of how city distribution grids should be progressively upgraded to accommodate DSRM are discussed, showing that effective decarbonization emerges mainly in mid-to-late upgrade stages. Distinct governing paradigms for allocating operational targets among communities, i.e., administrative equity versus mismatch-mitigation efficiency, creates trade-offs between temporal and spatial consistency of grid infrastructure upgrades. Figure 1 shows an illustration of the study. Table 1 summarizes the various domain models utilized in this study, along with their respective spatial and temporal resolutions.

Results

Demand-side resource endowments of Shenzhen's energy communities

The demand-side resource endowments of Shenzhen's CUs are shown in Fig. 2. The distributions of available RPV area, peak uncontrollable device (UD) load, peak SC load are aggregated from building-level profiles (see Methods), and the distribution of weekly P-PEV visits is identified from stay points of P-PEVs within a CU, as simulated by the P-PEV mobility model (see Methods). The maximum installable capacity of distributed BESS is assumed to be proportional to the number of buildings within a CU (see Methods), original distributions of the above assets are provided in Supplementary Fig. 8.

Figure 2a–d shows a spatial heterogeneity among different demand-side resources and the loads. The High-High (H-H) clusters of available RPV area (Fig. 2a) exhibit a peripheral-zonal pattern. The hotspots appear as large, continuous blocks primarily located in northwestern and southeastern Shenzhen, aligning with the characteristics of low-density districts. In contrast, peak UD load (Fig. 2c) and peak SC load (Fig. 2d) share a similar central-network pattern, with H-H clusters densely distributed along the urban core and major development spaces, reflecting the city's residential and commercial intensity. Notably, the H-H clusters of weekly P-PEV visits (Fig. 2b) show a hyper-centralized pattern, with the hotspots highly concentrated in the primary business districts (Nanshan, Futian, Luohu), indicating heavy traffic flows. This resource separation aligns with Ji et al.[27], who reported mismatched solar-potential and EV-demand distributions. The results of Global Moran's Indices[28] support the observations with the P-PEV visits exhibiting the strongest spatial autocorrelation (0.3178), the loads falling into an intermediate range (-0.09) and the RPV area showing the weakest clustering effect (0.0604). Detailed inner-district distributions of the above attributes are shown in Fig. 2e–h.

Allocating city mismatch across energy communities with distinct governing paradigms

To explore the city-level potential in reshaping load patterns via DSRM, the community-to-grid (C2G) framework is applied to community units (CUs). Given the heterogeneous resource endowments illustrated above, each CU schedules its internal demand-side resources including RPV, P-PEVs, BESSs, and SC DR (excluding winter) to align with allocated scheduling tasks. While C2G enables bidirectional power exchange, the maximum net feed-in power of a CU is constrained to not exceed its peak base load[16]. Notably, to

https://doi.org/10.1038/s41467-026-76799-4

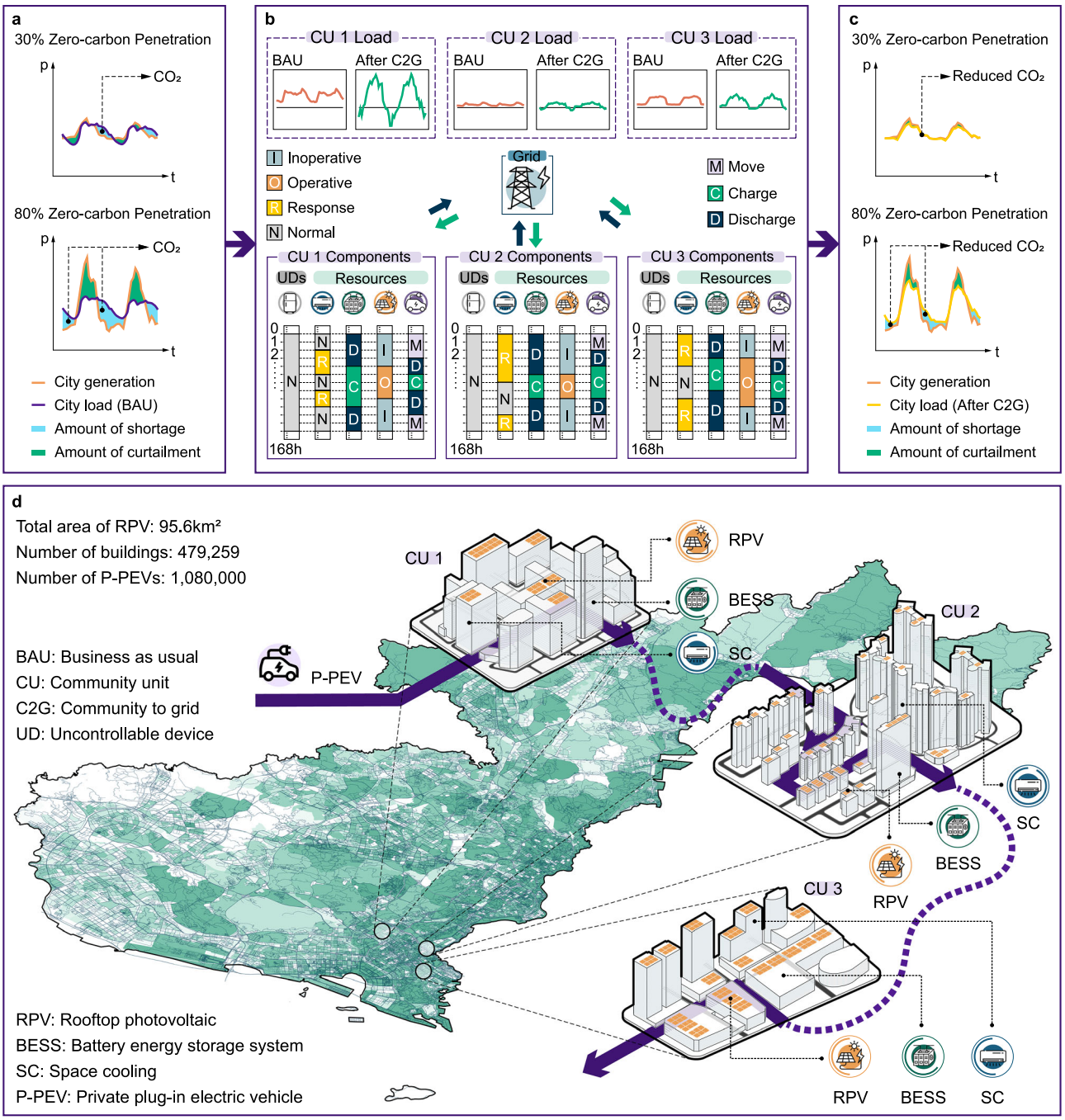


Fig. 1 | Scheduling demand-side resources in CUs for city electricity decarbonization. a The developing zero-carbon penetration intensifies the generation-demand mismatch. The mismatch is decomposed into amount of curtailment (AOC) and amount of shortage (AOS), and the latter requires being supplied by carbon-intensive backup power, yielding additional carbon emission. **b** City mismatch is distributed to CUs according to different allocation strategies (see Methods). In our C2G framework, CUs may bidirectionally exchange power with the grid under proper constraints. Each CU schedules the demand-side resources within to contribute to mismatch mitigation more or less. **c** After C2G, the city's generation-demand mismatch is effectively reduced compared with the BAU scenario. **d** Spatial illustration of C2G. Traveling trajectories of P-PEVs are decomposed into CUs. The stay duration of P-PEVs is scheduled for V2G in different CUs (see Supplementary Fig. 6). The Shenzhen administrative-boundary geometry was obtained from the ArcGIS Online feature layer "Population Density in Shenzhen Districts". The ArcGIS-derived map content is used herein under license. Copyright © 2026 Esri and its licensors. All rights reserved. The road-network shapefile was obtained from Geofabrik and is based on data © OpenStreetMap contributors, licensed under the Open Database License. Icons were adapted from resources available at Flaticon.com.

ensure fairness and energy stability of the collective P-PEV fleet across the city grid, the framework enforces that should not absorb net energy from the passing P-PEV population to facilitate its own scheduling, as presented in Methods, Eq. (22). The mechanism ensures that the total energy level of the city's P-PEV fleet remains stable over the optimization horizon.

Three scenarios are designed to represent different zero-carbon penetration levels: ZC 30, ZC 50, and ZC 80, where zero-carbon generation meets 30%, 50% and 80% of the city's total load, respectively. Before full zero-carbon generation is achieved, the planned generation mix includes coal power as base-load supply. The focus of this study is therefore not the planned emissions from coal

Table 1 | Spatial and temporal resolutions of different domain models used in this study

Domain model	Target asset	Spatial resolution	Temporal resolution
Building energy consumption	479,259 non-industrial buildings	Building-level, aggregated to CU	1 h
RPV generation	Deployable rooftop area	0.15 m pixel, aggregated to CU	1 h
RPV generation	Solar radiation and ambient temperature	City-level, Shenzhen	1 h
SC DR	Building thermal mass and adjustable load range	Building-level, aggregated to CU	1 h
P-PEV mobility and V2G activities	1.08 million P-PEVs	Individual stay segments, mapped to CU	1 h
C2G framework	Integrated demand-side resources	CU	1 h

CU community unit, *RPV* rooftop photovoltaic, *SC* space cooling, *DR* demand response, *P-PEV* private plug-in electric vehicle, *V2G* vehicle-to-grid, *C2G* community-to-grid.

generation, but the mismatch between the planned generation profile and the city load curve. This mismatch is decomposed in to the amount of curtailment (AOC), representing excess generation, and the amount of shortage (AOS), representing insufficient generation (see Fig. 1). AOS is assumed to be supplied by regulating gas power or external transmission[5], both of which introduce additional, unplanned carbon emissions to varying degrees (see Methods). To make a fair comparison across scenarios, an identical city load curve is maintained as the baseline.

Two strategies are developed to allocate the city-level mismatch among CUs, representing opposing governing paradigms. Flexibility quota allocation (FQA) simulates a resource-based policy prioritizing administrative equity. It assigns tasks to CUs proportional to their shares of available flexible resources. This strategy serves as a static baseline that assumes regulation capability is linearly equivalent to resource endowments. Potential-based allocation (PBA) represents an efficiency-driven paradigm. It distributes heavier burdens to CUs with superior regulation capabilities. By prioritizing system performance over simple proportional fairness, PBA aims to further unlock the city's potential of mismatch mitigation. By comparing these strategies, this study aims to quantify the value of exploiting resource heterogeneity versus adhering to rigid fairness. Detailed formulations are provided in Methods.

Baseline decarbonization performance under resource-based quotas

As the static baseline strategy, flexibility quota allocation (FQA) prioritizes administrative equity by assigning tasks based on predefined resource weights. Five FQA plans, P1-P5, are designed to represent different weighting preferences between the two primary flexibility sources: BESS and P-PEVs (see Eq. (45) in Methods). P1 represents a BESS-only policy, P5 represents an EV-only policy, and P2-P4 describe mixed BESS-EV allocations with gradually increasing EV weights. Seasonal operations are simulated to capture the effects of different load patterns and weather-dependent outputs of wind and solar.

Figure 3a–b shows that FQA reduces both the amount of curtailment (AOC) and the amount of shortage (AOS). As the zero-carbon penetration deepens, the business-as-usual (BAU) mismatch volume expands. Specifically, the summer BAU AOC/AOS increases from 145.4 GWh to 488.3 GWh. The winter BAU AOC surges from 137.7 GWh to 477.7 GWh, and BAU AOS rises from 137.7 GWh to 274.5 GWh. The discrepancy between the two metrics in winter ZC 80 stems from abundant zero-carbon generation. In summer, the best-performing FQA plans reduce AOC to 49.4–274.8 GWh and AOS to 88.0–262.9 GWh across zero-carbon penetration levels, corresponding to a CO_2 reduction of 21.1–70.7 kt through AOS mitigation (see Methods). In winter, FQA reduces AOC to 31.8–262.0 GWh and AOS to 71.9–124.1 GWh, corresponding to a CO_2 reduction of 24.2–47.2 kt. Prior studies[29,30] similarly show that coordinated flexible loads and V2G alleviate grid stress. Economic efficiency also improves as zero-carbon penetration increases. The reduction of curtailment/shortage cost (ROX cost), defined as the ratio of total DSRM cost to total mismatch reduction, decreases from 0.259–0.318 to 0.188–0.209 RMB per kWh in summer and from 0.243–0.355 to 0.226–0.292 RMB per kWh in winter. Based on reduction rates and ROX costs, P2 is selected as the representative FQA plan for subsequent comparisons. The results of transition-seasons (spring, fall) provided in Supplementary Table 30 show that FQA performance is robust across seasons, while the narrower adjustable range of SC DR makes its contribution season-specific.

The scheduled city load curves given by P2 are shown in Fig. 3c, d. The load curves of other plans are given in Supplementary Figs. 10–11. Regarding economic metrics, this study calculates two types of DSRM costs. Investment cost refers to the capital expenditure for deploying BESSs in buildings, converted into an equivalent weekly cost using an annual discount rate. Scheduling cost refers to operation-dependent subsidies paid to incentivize user participation in V2G and SC DR, with total costs varying according to subsidy levels and dispatched flexibility. The results given in Fig. 3 and Fig. 4 apply the highest subsidy (Sub4) to map the full extent of DSRM potential. The decomposition of investment or scheduling costs is given in Fig. 3e, revealing notable heterogeneity. Building-dense districts like Pingshan, Baon'an and Longgang incur the highest BESS investment costs, reaching a mean of 14,567–22,204 RMB (~2081–3172 USD) in summer and 17,913–22,684 RMB (~2559–3241 USD) in winter under ZC 80. In contrast, commercial hubs like Futian, Luohu and Nanshan dominate in V2G scheduling, spending on average 5453–15,207 RMB (~779–2172 USD) in summer and 8186–19,600 RMB (~1169–2800 USD) in winter. SC DR costs remain comparatively low, ranging between 29 and 1051 RMB (~4–150 USD).

Further excavating electricity decarbonization potential via efficiency-driven allocation

While FQA offers a conceptually intuitive policy framework, larger resource endowments do not necessarily translate into stronger regulation capability. This discrepancy stems from the complex interaction between CUs' heterogeneous internal resource constraints. To further unlock city-level mismatch mitigation, potential-based allocation (PBA) is developed as an efficiency-driven strategy. PBA uses dynamic programming to allocate larger scheduling tasks to CUs with stronger regulation potential, thereby prioritizing system performance over proportional resource fairness (see Methods).

Figure 4a compares PBA with FQA, P2 in terms of relative changes in maximum and mean district-level total costs. PBA requires higher costs in the early transition stage due to the deep excavation of regulation capabilities. Under ZC 30, mean district costs increase by 74.9–332.1% in summer and 20.6–39.2% in winter, while maximum costs change by −9.4% to 151.1% and 0.3–67.7%, respectively. As zero-carbon penetration increases, this cost premium narrows. Under ZC 80, mean cost changes fall to −30.6% to 48.5% in summer and −6.5 to 17.3% in winter, with maximum cost changes of −23.8 to 63.7% and −3.3 to 13.5%. These results indicate that PBA becomes more economically competitive under high zero-carbon penetration.

https://doi.org/10.1038/s41467-026-76799-4

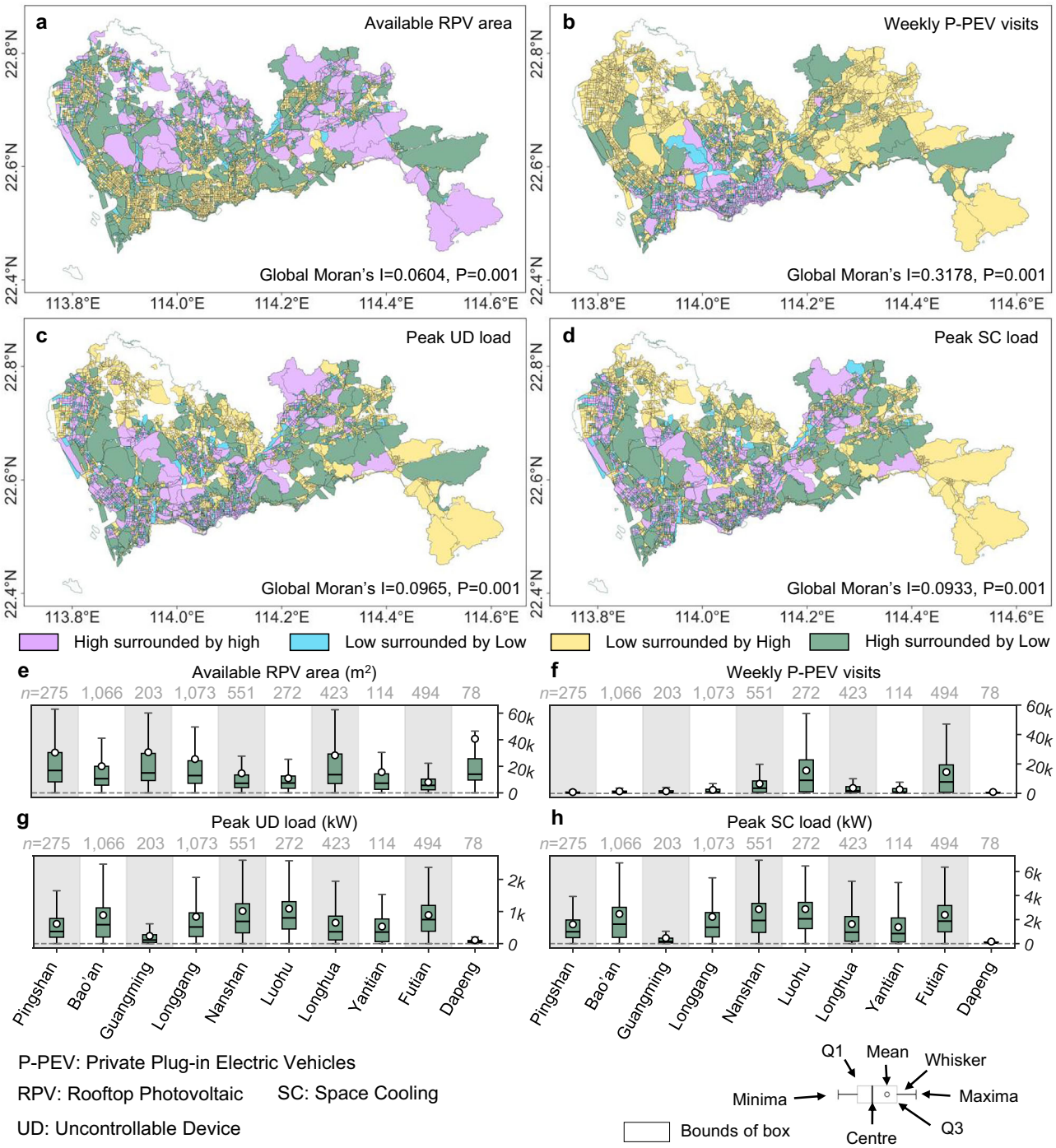


Fig. 2 | Demand-side resource endowments of Shenzhen's CUs. a–d Local Moran's I statistics[68] of available RPV area, weekly P-PEV visits, peak UD load, peak SC load, respectively. Global Moran's I values[28] are calculated using a k-nearest-neighbor spatial weight matrix (k = 5). Statistical significance of Global and Local Moran's I statistics is evaluated using two-sided permutation tests with 999 randomizations. No correction for multiple comparisons is applied. Exact permutation *P* values are reported. Although the maps render all 4549 CUs, some smaller CUs are difficult to distinguish. A zoomed-in schematic is given in Supplementary Fig. 9. **e–h** district-level aggregated box plots of available RPV area, weekly P-PEV visits, peak UD load and peak SC load, respectively.

Figure 4b compares the performance of the two strategies. The higher expenditures observed in Fig. 4a translate into deeper decarbonization, yielding notably lower AOS across all scenarios. Specifically, compared with FQA, P2, PBA lowers the metrics to 16.4 GWh (−83.1%), 73.3 GWh (−50.0%), 222.1 GWh (−15.5%) in summer, and to 49.1 GWh (−32.9%), 101.7 GWh (−9.9%), 114.3 GWh (−11.3%) in winter. In terms of decarbonization, PBA achieves a CO_2 reduction of 47.4–83.6 kt and 32.5–50.3 kt in both seasons, respectively. This performance gap quantifies the value of exploiting resource heterogeneity of CUs. The spring and fall experiments in Supplementary Table 31 show the same direction, with PBA further reducing AOS by 6.9–68.7% in spring and 5.6–56.4% in fall relative to FQA. Load curves and cost distributions of PBA are provided in Supplementary Figs. 12–13.

While PBA contributes marginally or negatively to AOC mitigation (altering metrics by −9.4% to +12.5%), its primary advantage lies in

https://doi.org/10.1038/s41467-026-76799-4

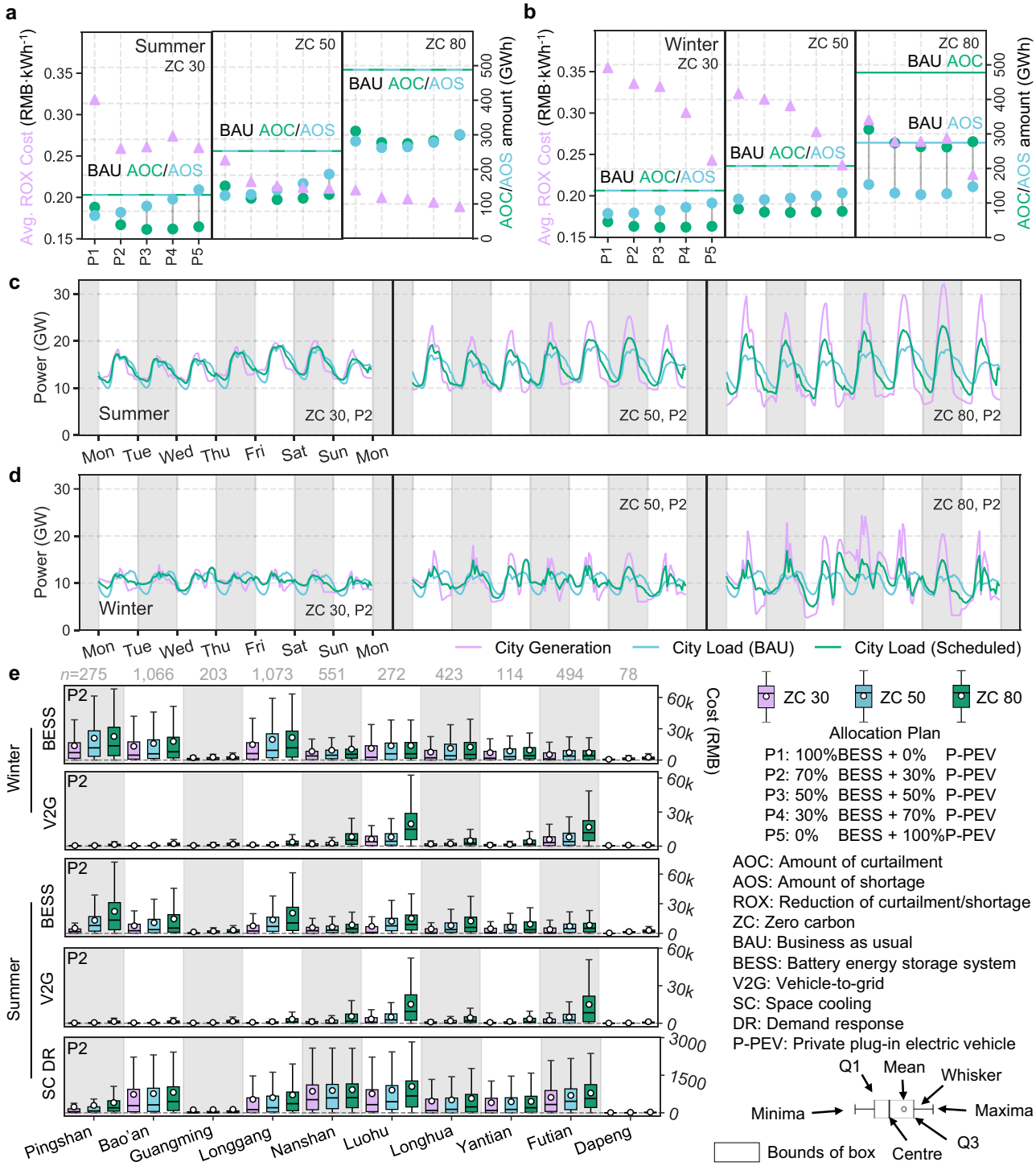


Fig. 3 | Decarbonization potential under flexibility quota allocation. **a**, **b** Comparison of seasonal AOC, AOS and average ROX Cost among the BAU scenario and different allocation plans. **c**, **d** Seasonal power curves of city generation, city load (BAU) and city load (Scheduled). **e** Seasonal inner-district distribution of economic costs paid for investing or scheduling BESS, V2G and SC DR.

shortage mitigation. Additionally, the gap in average ROX cost between PBA and FQA narrows as zero-carbon increases, reaching +41.4% (ZC 30), +18.6% (ZC 50), +0.5% (ZC 80) in summer, while shifting to +11.0% (ZC 30), +1.6% (ZC 50) and +1.4% (ZC 80) in winter, which is consistent with the trend observed in Fig. 4a.

Finally, the distributional equity of system costs is evaluated using the Gini coefficient, as shown in Fig. 4c. Although FQA is designed as a uniform resource-based rule to prioritize administrative equity, it does not necessarily produce a more balanced economic burden. In the summer ZC 30 scenario, FQA reaches a Gini coefficient of 0.702, significantly higher than the 0.598 of PBA. Under deeper ZC penetrations, the differences remain marginal or mixed. The results of spring and fall provided in Supplementary Table 31 show that the phenomenon is robust across seasons. The mechanism is that a fixed proportional rule may assign tasks to communities where the low-cost resources such as V2G and SC DR are insufficient, forcing greater reliance on high-cost BESS investment and concentrating costs. By contrast, PBA can shift part of the burden toward communities with stronger low-cost

https://doi.org/10.1038/s41467-026-76799-4

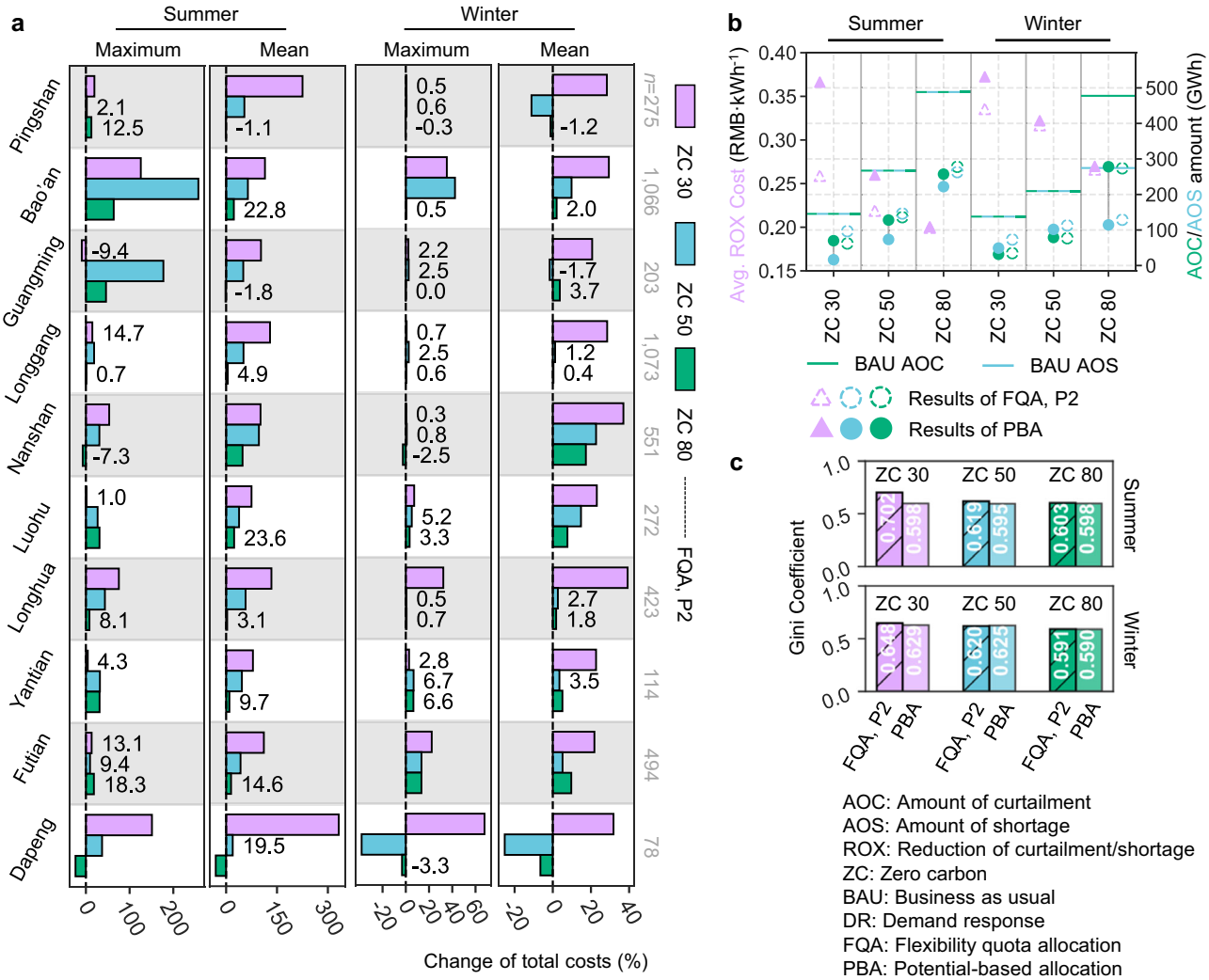


Fig. 4 | Decarbonization potential under potential-based allocation. a District-level distributions of the maximum, mean values of total costs. The panel illustrates the relative change rates of PBA to FQA, P2. **b** Comparison of seasonal AOC, AOS and average ROX Cost between PBA and FQA, P2. **c** Comparison of the Gini coefficients of total costs between PBA and FQA, P2.

flexibility, although this redistribution effect weakens when high zero-carbon penetration makes the tasks generally more difficult. This finding is consistent with prior energy-justice studies[31,32], which show that uniform policy treatment does not automatically lead to equitable outcomes when initial resource conditions differ across communities. A detailed mechanism analysis is provided in Supplementary Note 1, Supplementary Tables 1–4.

Economic trade-offs for demand-side resource management

Subsidy levels determine the unit cost paid to P-PEV users or buildings for participating in V2G or SC DR[17,33] (see Methods). A higher subsidy amplifies the price signal to incentivize a broader population of P-PEVs and buildings. While previous analysis in Fig. 3 and Fig. 4 use the highest tier (Sub4) to map the full extent of city community-to-grid (C2G) potential, this section investigates the practical trade-offs between regulation performance and economic efficiency, using the ZC 80 scenario as an example.

For the FQA case in Fig. 5a, higher subsidy levels mobilize broader flexibility resources, making the amount of shortage (AOS) monotonically decrease from 369.3 GWh to 262.9 GWh in summer, and from 185.6 GWh to 128.9 GWh in winter. However, the average reduction of curtailment/shortage cost (ROX cost) exhibits a U-shaped trajectory under both seasons, indicating a threshold of diminishing returns locating at Sub2 or Sub3. Similar trends are observed for the PBA case in Fig. 5b. The total costs are decomposed in Fig. 5c, Fig. 5d. Compared to the maximum intensity (Sub4), adopting Sub3 reduces total costs to 90.6–93.1% across all scenarios. Correspondingly, AOS increases by 4.0–9.2% and AOC increasing only by 0.1–2.1%. This indicates a practical threshold beyond which additional subsidies yield limited regulation gains. The spring and fall results in Supplementary Tables 33–34 confirm that this intermediate-subsidy threshold is robust across seasons, although the absolute SC DR subsidy costs remain season-specific because cooling-related flexibility is weaker in transition seasons than in summer. Similar diminishing returns have been reported in V2G participation studies, where higher compensation attracts more participants but the marginal flexibility benefit gradually declines[34].

Spatiotemporal trade-offs in progressive grid infrastructure upgrades

While the proposed community-to-grid (C2G) framework incorporates the feed-in limits[16] of community units (CUs), the scheduled load profiles inevitably exhibit different dynamics with steeper ramp rates[16] compared to the BAU loads, particularly under high zero-carbon penetration scenarios where rapid regulation is required. Therefore, the city distribution grids still require infrastructure upgrades to

https://doi.org/10.1038/s41467-026-76799-4

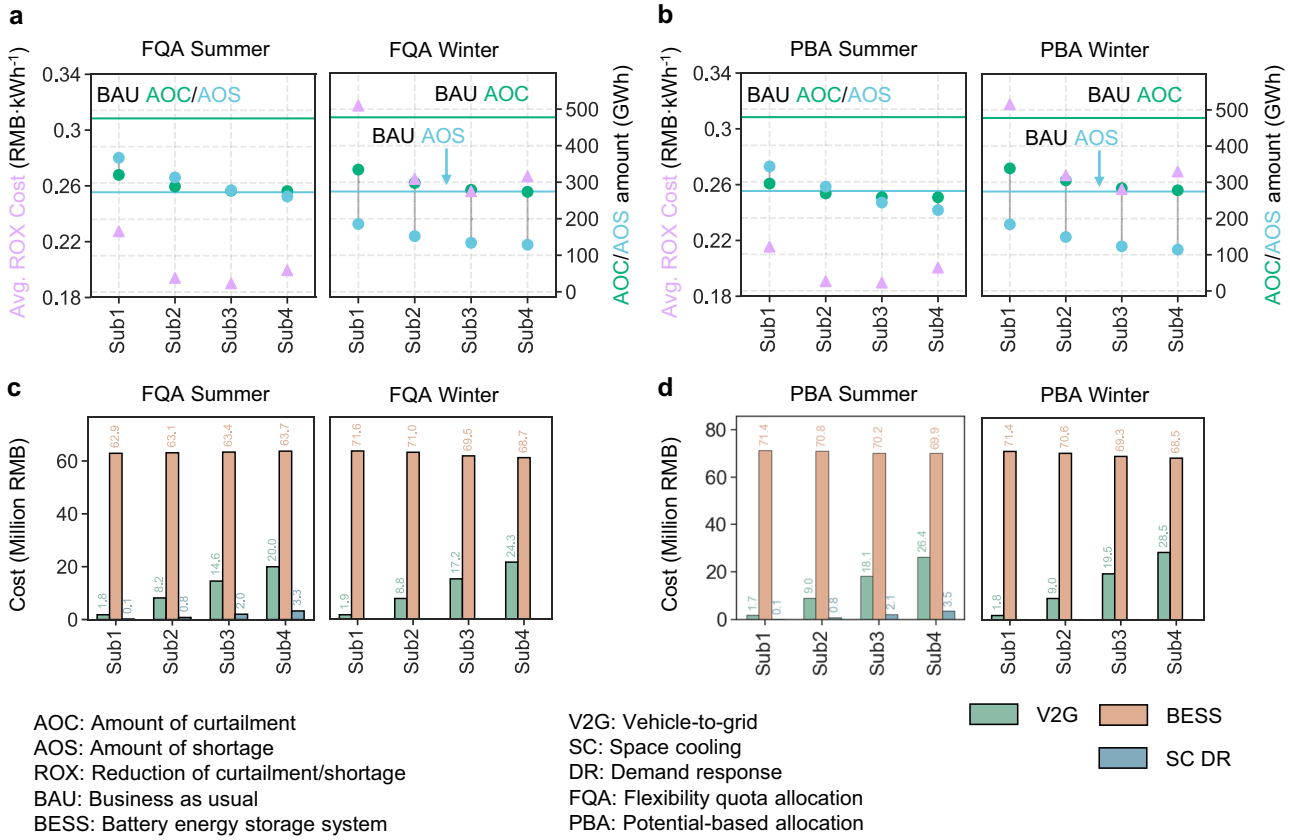


Fig. 5 | Community-to-grid performance and corresponding system costs with various subsidy levels. a, **b** Metrics of AOC, AOS and average ROX cost of FQA, P2 and PBA, respectively. **c**, **d** Subdivided costs of V2G, SC DR subsidies and BESS investment of FQA, P2 and PBA, respectively. Detailed mechanisms of subsidy levels are given in Methods.

accommodate the intensified fluctuations. This section correlates the calculated ramp rate escalation with each CU's contribution to mismatch mitigation, proposing a referenced, progressive upgrade path for the city.

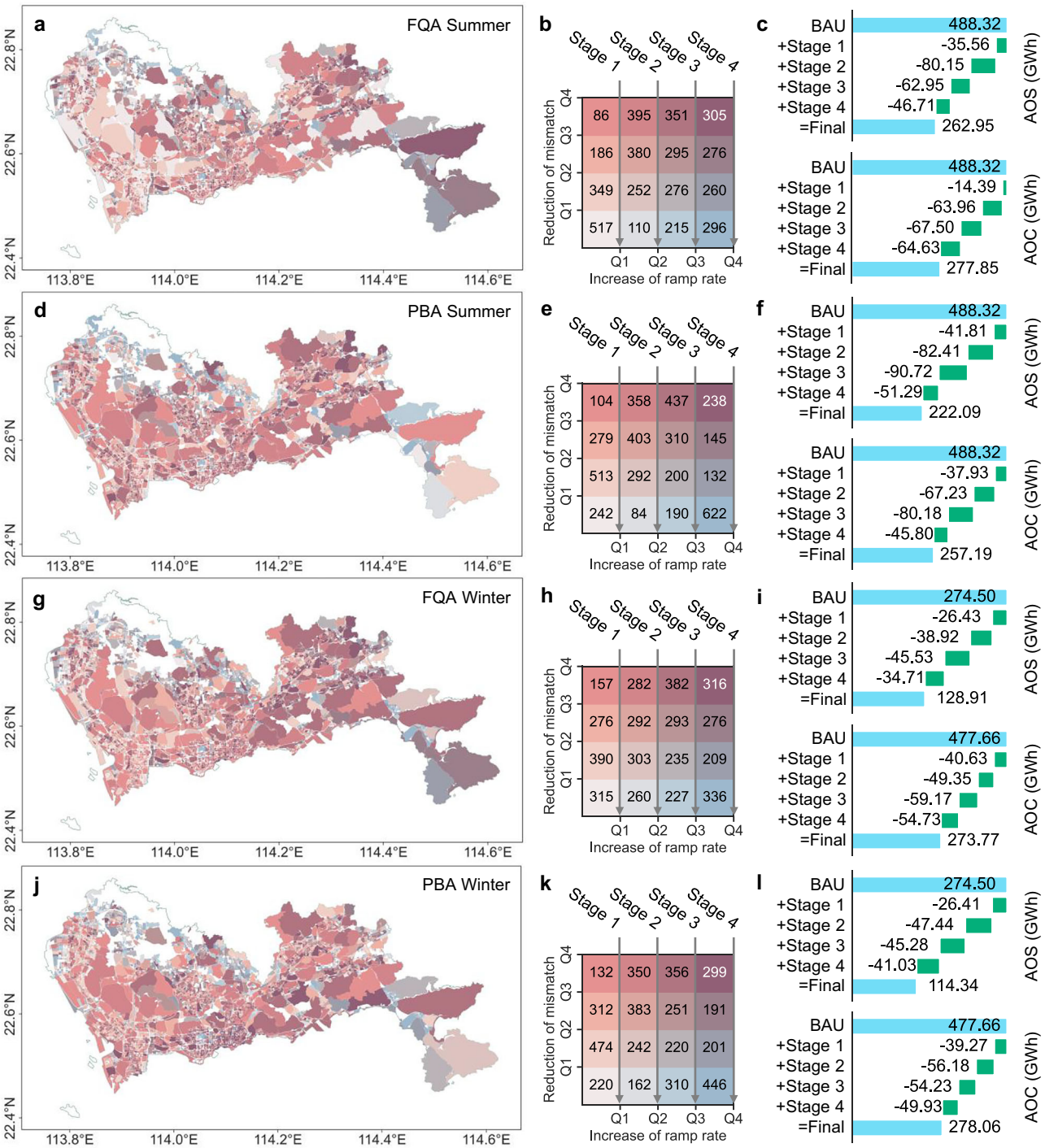
The results under ZC 80 are shown in Fig. 6. The city's reduction of amount of curtailment (AOC), amount of shortage (AOS) is attributed to each CU to quantify its contribution to mitigating generation-demand mismatches. Detailed attribution mechanisms and results are introduced in Supplementary Note 2, Supplementary Tables 5–6, Supplementary Figs. 1–4. Meanwhile, the grid impact is evaluated using the increase of ramp rate, defined as the multiple of the C2G-involved ramp rate relative to the BAU baseline. By dividing the two metrics into quartiles, a bivariate framework is constructed to map the trade-off between upgrade difficulty (increase of ramp rate) and system rewards (reduction of mismatch), as shown in Fig. 6b, e, h, k. A "low-hanging fruit" strategy is adopted to prioritize upgrades that are easier to implement yet offer higher returns, according to four progressive stages defined based on the quartiles of ramp rate increase. Within each stage, priority is further assigned to CUs with larger contributions to mismatch reduction. The corresponding spatial distributions are visualized in Fig. 6a, d, g, j.

The stepwise breakdown in Fig. 6c, f, i, l shows that the initial upgrade stage contributes the weakest mitigation effect for both AOS and AOC. Across the four seasonal-allocation cases, Stage 1 reduces AOS by only 26.4–41.8 GWh and AOC by 14.4–40.6 GWh, whereas larger reduction generally emerge after Stage 2 and Stage 3 communities are included. This pattern suggests that the easiest communities to upgrade from a ramp rate perspective are not necessarily those with the strongest dispatchable flexibility. Detailed analysis in Supplementary Note 3, Supplementary Tables 7–9 and Supplementary Fig. 5 show that Stage 1 communities often retain high baseline loads but have limited P-PEV and BESS resources, so the ability to regulate their own load curves remains constrained. In addition, their received signals of upward and downward adjustments from the assigned tasks are often imbalanced, which restricts charge-discharge cycling of P-PEVs and BESSs. Although this imbalance is less strongly associated with Stage 1 performance than resource endowment, it still helps explain the limited early-stage mitigation effect, as shown in Supplementary Tables 10–12. Mid-to-late stages involve deeper flexibility activation, allowing stronger load shifting and larger mismatch mitigation. A not fully equivalent comparison can be drawn from a V2G-grid upgrade study[35], which also suggests that early or incremental actions alone may be insufficient.

To validate the spatial characteristics presented in Fig. 6a, d, g, j, the Global Moran's Indices[28] are compared across different scenarios in Table 2. The reduction of mismatch exhibits consistently significant positive spatial autocorrelation regardless of the allocation strategy ($I \approx 0.16 - 0.20, P < 0.001$). Regarding the increase of ramp rate, however, FQA results in a spatially random distribution (lower or non-significant indices in summer), while PBA induces a significant spatial clustering of the metric across all four seasons, combining the spring and fall results in Supplementary Table 35. The magnitude of this clustering is season-specific, e.g., spring has higher Moran's Indices than summer under PBA. Since it serves as an indicator for upgrade difficulty, PBA may facilitate a more spatially unified policy implementation at contiguous zones rather than scattered randomly.

While PBA offers better spatial consistency in single-season upgrade paths, FQA outperforms in cross-season continuity, namely temporal consistency. The metric is quantified by calculating the number of CUs that remain in the same upgrade stage across all

https://doi.org/10.1038/s41467-026-76799-4



FQA: Flexibility quota allocation
PBA: Potential-based allocation
AOC: Amount of curtailment
AOS: Amount of shortage
BAU: Business as usual
Q1, Q2, Q3, Q4: 25th, 50th, 75th, 100th percentile

Fig. 6 | Progressive grid upgrades under FQA, P2 and PBA, decomposed into stages. a, **d**, **g**, **j** Spatial distributions of CUs with different quartile combinations of reduction of mismatch and increase of ramp rate. **b**, **e**, **h**, **k** Quartile combinations of reduction of mismatch and increase of ramp rate, with the number of CUs falling into, respectively. The upgrade stages are divided according to the increase of ramp rate, from Q1 (easy) to Q4 (difficult). **c**, **f**, **i**, **l** Waterfall plots indicating the effects of reducing AOS and AOC at each stage.

seasons. Here, since FQA allocates tasks based on static resource capacities, it yields a more stable upgrade path, making 840, 369, 317, 754 CUs (out of ~1137 per stage) retain their respective classifications (Stage 1–4) across seasons. Conversely, PBA, being sensitive to the dynamic variations in seasonal generation-demand profiles, results in greater temporal fluctuation. The number of overlapping CUs drops to 461, 168, 176, and 484, respectively. This reveals a spatiotemporal trade-off where PBA is better for zonal construction and FQA outperforms in long-term planning stability. Policymakers should therefore balance the need for spatially concentrated engineering works against seasonally robust upgrade plans.

To make these upgrade stages more interpretable for municipal planning, this study further links ramp-rate-based stages to possible transformer capacity upgrades, which are estimated from changes in

Table 2 | Global Moran's I statistics[29] of increase of ramp rate and reduction of mismatch across all scenarios. *k* denotes the number of neighbors in k-nearest-neighbor (kNN) algorithm

Global Moran's Indices[29] of the increase of ramp rate			
Scenario	**3 nearest neighbors**	**5 nearest neighbors**	**7 nearest neighbors**
FQA P2, ZC 80, Summer	0.0087, $P = 0.060$	0.0110, $P = 0.046$	0.0086, $P = 0.049$
PBA, ZC 80, Summer	0.0780, $P = 0.004$	0.0702, $P = 0.003$	0.0587, $P = 0.001$
FQA P2, ZC 80, Winter	0.0134, $P = 0.025$	0.0113, $P = 0.049$	0.0086, $P = 0.052$
PBA, ZC 80, Winter	0.0475, $P = 0.003$	0.0474, $P = 0.002$	0.0446, $P = 0.001$
Global Moran's Indices[29] of the reduction of mismatch			
Scenario	3 nearest neighbors	5 nearest neighbors	7 nearest neighbors
FQA P2, ZC 80, Summer	0.1968, $P = 0.001$	0.1852, $P = 0.001$	0.1740, $P = 0.001$
PBA, ZC 80, Summer	0.1685, $P = 0.001$	0.1675, $P = 0.001$	0.1629, $P = 0.001$
FQA P2, ZC 80, Winter	0.1945, $P = 0.001$	0.1990, $P = 0.001$	0.1967, $P = 0.001$
PBA, ZC 80, Winter	0.1730, $P = 0.001$	0.1800, $P = 0.001$	0.1797, $P = 0.001$

Statistical significance of Global Moran's I is assessed using two-sided permutation tests with 999 randomizations. Exact permutation *P* values are reported. No correction for multiple comparisons is applied. The results demonstrate robustness across varying k-nearest-neighbor parameters ($k = 3,5,7$).
FQA flexibility quota allocation, *PBA* potential-based allocation, *ZC* Zero carbon.

peak active power under a standard safety margin and power factor assumption. Detailed assumptions and results are provided in Supplementary Note 4, Supplementary Table 13. In summer, when community loads approach their annual peaks, the estimated total transformer upgrade capacity reaches approximately 4500–4725 MVA, and mid-to-late stages generally involve broader or larger-capacity upgrades than the initial stage. Regarding other practical measures, potential feeder-level measures may include main-line capacity expansion, terminal-voltage monitoring, and protection devices compatible with bidirectional power flows; voltage-control solutions may include software optimization and static var generators.

Temporal data alignment and system robustness to load variation

The datasets employed in this study do not strictly align within a single calendar year. In long-term urban energy-system planning, strict calendar-year consistency across multi-source datasets is difficult to achieve, especially when fine-grained building, mobility, photovoltaic, and city-load data are collected through different channels. This study therefore prioritizes the granularity of the load profile, following common practice in scenario-based energy system analyses[35,36]. To test whether this choice affects the main findings, sensitivity analyses are conducted under both uniform and sector-differentiated load variation assumptions. The uniform cases cover load decrease and increase levels from 92% to 125% of the baseline, while the non-uniform cases distinguish faster growth in building and non-building demand. Across these scenarios, the reduction ratios of the amount of shortage (AOS) and the amount of curtailment (AOC) remain stable, confirming the robustness of the conclusions. Sensitivity results are provided in Supplementary Note 5, Supplementary Tables 14–21.

Seasonal stability assumption of private plug-in electric vehicle mobility patterns

The P-PEV trajectory dataset used to parameterize the mobility and V2G coupled framework (MOVC)[17] covers October to December, representing a single-season observation of vehicle mobility. Accordingly, this study assumes that the general mobility characteristics of P-PEVs, including stay intervals and inter-community travel patterns, remain broadly stable across seasons. Similar assumptions have been adopted in EV operation and infrastructure-planning studies that infer long-term scenarios from limited mobility records[37,38].

If seasonal mobility variations occur, the results would mainly be affected through two aspects. First, changes in stay duration and arrival-departure timing would alter V2G availability. Longer stays during mismatch-critical hours could strengthen AOC/AOS mitigation, whereas shorter or more fragmented stays would reduce flexibility. Second, seasonal spatial redistribution of trips would shift P-PEV flexibility among community units (CUs), potentially changing local performance and the priority of grid infrastructure upgrades.

Annual robustness considering transition-season scenarios

To consider seasonal variations more comprehensively, the analysis is extended to transition-season weeks in spring and fall, in addition to summer and winter cases. These additional scenarios capture intermediate climate conditions, under which SC DR remains available but its adjustable range is narrower than in summer. Consequently, SC DR contributes less in transition seasons than during summer periods, with correspondingly lower SC DR subsidy costs. The broader conclusions remain stable after introducing these annual considerations. Specifically, potential-based allocation (PBA) continues to provide stronger generation-demand mismatch mitigation than flexibility quota allocation (FQA), the most cost-effective subsidy settings remain at intermediate levels, and the grid infrastructure results preserve the same policy interpretation, with PBA showing stronger spatial clustering and FQA yielding more temporally stable upgrade paths. Detailed quantitative results are provided in Supplementary Figs. 14–18, Supplementary Tables 30–35.

Participation levels and scope of demand-side resource management engagement

The main experiments assume citywide participation of all CUs in DSRM, while the user participation mechanism regulates flexible assets within each CU. Specifically, subsidy levels determine the participation of P-PEV users in V2G scheduling and buildings in SC DR, as illustrated in Supplementary Figs. 6–7. A supplementary sensitivity analysis further examines partial CU participation by randomly selecting 20% and 60% of CUs. The results show that reduced CU participation does not always weaken performance under ZC 30 and ZC 50, because fewer participating CUs receive larger mismatch-allocation tasks and therefore activate stronger local flexibility responses. However, under ZC 80, partial participation generally performs worse than the full-participation baseline, as the limited resource endowment constraints the upper bound of achievable flexibility. More realistic partial participation would require explicit modeling of CU selection order and fairness implications, which lies beyond the present scope. Detailed results are provided in Supplementary Note 6, Supplementary Data 1–3, Supplementary Tables 22–26.

Implications of broader demand-side management and demand response strategies

The DSRM concept in this study is closely related to but more specifically configured than the demand-side management (DSM) and demand response (DR) concepts discussed in existing literature[39,40]. While DSM broadly covers reserve provision, strategic load planning, energy efficiency, and DR programs, DR usually refers to specific operational mechanisms, namely incentive-based and price-based load adjustment. The subsidy modeled in this study is regarded as incentive-based.

Several DSM strategies are not explicitly investigated in this study. Their application may influence system performance in the following ways. Reserving part of BESS or P-PEV capacity for ancillary services would reduce the flexibility available for AOC/AOS mitigation, although it could improve system reliability. Price-based DR may lower direct incentive payments, but it would introduce greater behavioral uncertainty and weaker controllability than the incentive-based mechanism modeled here. Energy-efficiency improvements, an example of which is given in Supplementary Table 36, would reduce baseline uncontrollable loads and SC demand, thereby lowering total costs and V2G/SC DR subsidy costs while slightly increasing the reduction of curtailment/shortage costs (ROX costs).

Key policy messages

This study offers several policy implications for municipal planners. If allocation strategies are adjusted during the zero-carbon transition, PBA may preferable at earlier stages because of its stronger mismatch mitigation performance and greater economic equity, whereas FQA allocation may be more suitable at higher zero-carbon penetration levels because of its transparent decision rules and greater seasonal stability in grid upgrade planning. Subsidy design should also be phased rather than uniformly maximized, as intermediate subsidy levels may preserve most mismatch mitigation benefits while reducing total costs. To improve economic equity, more targeted subsidies may be needed to support resource-poor communities in financing high-cost BESS investments. Before policy implementation, municipal planners should also evaluate operational synergies across communities, which are not considered in this study. Inter-community energy sharing mechanisms should be established to encourage active resource sharing among neighboring CUs, particularly for communities at early upgrade stages, since their local flexibility is insufficient.

Discussion

This study proposes a community-to-grid (C2G) framework for granular assessment of DSRM potential in city electricity decarbonization. Using Shenzhen as a case study, the framework captures the spatial heterogeneity of demand-side resources across community units (CUs) and evaluates two governing paradigms: flexibility quota allocation (FQA), which emphasizes administrative equity, and potential-based allocation (PBA) which prioritizes mismatch mitigation efficiency. The results reveal substantial city-scale decarbonization potential from coordinated demand-side resources. Under FQA, the amount of curtailment (AOC) is reduced by 95.5–225.4 GWh and the amount of shortage (AOS) by 57.4–213.5 GWh, corresponding to 21.1–70.8 kt of CO_2 reduction. By further exploiting heterogeneous resource endowments, PBA increases projected emission reductions to 32.5–83.6 kt while maintaining comparable economic equity. The most cost-effective subsidy can reduce total costs to 90.6–93.1%, with AOS increases of 4.0–9.2% and AOC increases of 0.1–2.1%. For grid infrastructure upgrades, results show that the easiest upgrades have limited effects of mismatch mitigation, whereas larger reductions generally emerge in the mid-to-late upgrade stages. A spatiotemporal trade-off is observed in policy implementation: while PBA offers better spatial consistency for targeted zonal upgrades, FQA provides better temporal stability across seasons.

The main contribution of this study lies in connecting fine-grained demand-side resource modeling with city electricity decarbonization policy analysis. Compared with prior work[17] focusing on V2G, the C2G framework co-optimizes multiple heterogeneous demand-side resources considering local operational constraints. A noteworthy feature is the decoupling of P-PEV travel-charge patterns into CUs, which embeds user-centric mobility predictions[17] into community-centric scheduling. This design avoids reliance on predefined probability distributions for simplifying P-PEV behavior[41], ensures that incentive-driven V2G participation is consistently represented across all CUs, and enables parallel computation for scheduling more than one million vehicles. Beyond quantifying DSRM potential, this study links operational scheduling outcomes to policy-relevant dimensions, including administrative equity, mismatch mitigation efficiency, economic burden, subsidy design, and progressive grid infrastructure upgrade paths. These extensions help translate fine-grained analysis into practical guidance for municipal decision-makers facing both decarbonization targets and distribution-grid constraints.

It must be acknowledged that several limitations exist in the study. First, each CU is modeled as an independent unit interacting with the grid, without operational coupling among neighboring CUs. This decoupled design supports parallel city-scale optimization but overlooks cross-CU synergies, such as local energy exchange or surplus resource sharing between adjacent communities. It also does not jointly optimize P-PEV mobility and availability across CUs. Therefore, the results should not be interpreted as an absolute citywide optimum. Incorporating cross-CU exchange and coupled heating/cooling networks may alter local regulation actions, overall DSRM potential, and grid upgrade trajectories. Second, both FQA and PBA allocate city-level mismatch to CUs through linear weights, which may assign regulation targets that are poorly aligned with a CU's load shape, creating imbalanced opportunities for upward and downward adjustment and limiting the activation of P-PEVs and BESSs, as illustrated in Supplementary Fig. 5 and Supplementary Tables 9–12. Non-linear or network-constrained allocation could offer regulation targets with better load alignment, further activating the resources within communities, especially the ones with inferior performance in early upgrade stages. However, the interpretability of such measures requires further investigation.

Other limitations are summarized as follows. First, this study uses hypothetical generation mix due to the lack of data, and the estimation of carbon reduction from AOS relies on simplified assumptions. A precise quantification requires detailed data on urban thermal units and external power transmission. Second, the proposed scenarios do not account for extreme weather events or natural disasters, which provide insights for grid resilience[42]. Third, the community-centric perspective is difficult to track certain user-centric information, such as individual battery degradation[17]. Finally, this study does not discuss the detailed impact of market mechanisms on economic costs, such as profits of RPV feed-in, since C2G would significantly alter the generation-demand economics.

Future research can be extended in several directions. First, synthesizing the single-scenario, single-season upgrade paths into a multi-scenario, all-season analysis would create a roadmap consistent in decades, offering robust long-term guidance for specific cities. Second, future work could shift focus from system potential excavation to economic profitability, analyzing the profit margins of CUs to inform market mechanism design. Third, as this study focuses on generation-demand mismatch mitigation rather than the maximization of RPV self-consumption, future works could discuss the synergies or trade-offs between distributed PV absorption and the broader goal of city electricity decarbonization.

Methods

Datasets

In this study, the geometric data of 577,480 individual buildings in Shenzhen is collected from Amap[43,44]. Warehouse buildings are excluded, leaving 479,259 buildings for further analysis. Weather data for the EnergyPlus simulations are derived from Climate.Onebuilding[44,45]. Building types are identified from the land planning information provided by the Shenzhen Municipal Bureau of Planning and Natural Resources[44,46].

The 2022 Shenzhen P-PEV Trajectories Dataset[17] provided by the Shenzhen Municipal Transport Bureau is used to model P-PEV mobility. The dataset collects 9,108,081 location records via Bluetooth devices from 36,932 P-PEV users primarily active in Shenzhen. The dates start from October 1, 2022 and end in December 31, 2022. Each record contains the information of anonymous user ID, timestamp, duration, latitude and longitude. The data is used to extract stay/movement information and to generate user-specific behavior parameters for the Timegeo[47]-based mobility model.

The assumptions of city electricity generation profiles are sourced from the power development reports published by China Southern Power Grid[48,49]. The share of (Nuclear, PV, Wind) power under ZC30, ZC50, ZC80 is set as (10%, 10%, 10%), (18%, 22%, 10%) and (33%, 37%, 10%), respectively. Due to the limited accessibility of detailed capacity and operational data for individual generation units in Shenzhen, the unit commitment in this study is constructed from an energy-balance perspective. Nuclear and planned coal generation are modeled as constant base-load supply, whereas wind and PV generation are modeled as variable supply. Their combined output is constructed to meet total daily demand. Any hourly amount of shortage (AOS) caused by temporal mismatch is assumed to be supplied by gas power or external transmission, both of which introduce additional unplanned emissions. The calculation method for PV power will be introduced in the following section. The calculation for wind power generation utilizes results from an open-source platform[50].

Thermal simulation parameters are extracted from Design Standard for Energy Efficiency of Public Buildings[51] and Design Standard for Energy Efficiency of Residential Buildings[52], published by the Shenzhen Housing and Construction Bureau. The parameters include window-to-wall ratio, heat transfer coefficient, solar heat gain coefficient, power density of different devices, per capita floor area, and operation schedule. The details of the above parameters and other necessary assumptions are listed in Supplementary Tables 37–43.

The 2021 Shenzhen electricity load profile provided by China Southern Power Grid is used to obtain the city's original overall load. The data contains hourly load values for Shenzhen over the entire year. A week's values of load data is selected for each season.

The RPV area in Shenzhen is extracted from the high-resolution imagery of Google Earth Satellite[53,54]. The spatial resolution is set as 0.15 m.

The geometric data of community units (CUs) is provided by Wei et al.[26]. 4549 CUs are identified, each of which contains at least one of the 479,259 individual buildings extracted above. After combining the mobility patterns of P-PEVs, there are 4134 CUs with at least one record of P-PEV visit and 415 CUs without one.

Building energy consumption simulation

Building materials are modeled according to the ASHRAE 198.1–2020 standard, which provides material libraries specific to different climate zones[44,55]. The height of each floor is assumed to be 3 m according to the AMap data[43]. This study uses Ladybug Tools[56] to generate building energy consumption profiles by embedding physical parameters and various operation schedules into the building models. EnergyPlus[57] is used to output hourly building energy consumption profiles[44,58].

RPV generation modeling

The extraction of available RPV area follows the settings of Zhu et al.[44] and Wei et al.[26]. The overall available area is identified as 95.6 km^2, with the distribution shown in Supplementary Fig. 8. The calculation of RPV generation is given in Eq. (1) [26,59]:

$$P_{\mathrm{RPV}} = \eta_{\mathrm{RPV}} S_{\mathrm{RPV}} I_{\mathrm{R}} (1 - 0.005(T_{\mathrm{out}} - 25)) \tag{1}$$

where η_{RPV} is the conversion efficiency set as 0.157, S_{RPV} is the panel area (m^2), I_{R} is the solar radiation (kW · m^{-2}) and T_{out} is the outdoor air temperature (°C). The data of I_{R} and T_{out} are sourced from EnergyPlus[57]. To ensure the consistency of PV generation patterns, the centralized PV generation is computed identically as described in Eq. (1). It is assumed that 30%, 50%, 80% of RPV area is deployed with PV panels under ZC 30, ZC 50, ZC 80, respectively.

Space cooling demand response modeling

It is assumed that the SC load $P_{\mathrm{SC}}(t)$ of a building is determined by the building's thermal dynamics and mainly by the indoor air temperature $T_{\mathrm{in}}(t)$, which is updated based on the net heat gain and the building's thermal capacity.

The total heat gain rate $Q_{\mathrm{gain}}(t)$ (in Watts) is the sum of four components as Eq. (2):

$$Q_{\mathrm{gain}}(t) = Q_{\mathrm{cond}}(t) + Q_{\mathrm{solar}}(t) + Q_{\mathrm{int}}(t) + Q_{\mathrm{vent}}(t) \tag{2}$$

where $Q_{\mathrm{cond}}(t)$ is the heat gain from thermal conduction through the building envelope, $Q_{\mathrm{solar}}(t)$ is the solar heat gain through windows considering both direct heating and delayed release from thermal mass, $Q_{\mathrm{int}}(t)$ is the internal heat gain from occupants, lighting and equipment, and $Q_{\mathrm{vent}}(t)$ is the heat gain from ventilation and infiltration.

$Q_{\mathrm{cond}}(t)$ is computed as Eq. (3):

$$Q_{\mathrm{cond}}(t) = (U_{\mathrm{wall}} A_{\mathrm{wall}} + U_{\mathrm{roof}} A_{\mathrm{roof}} + U_{\mathrm{win}} A_{\mathrm{win}})(T_{\mathrm{out}}(t) - T_{\mathrm{in}}(t-1)) \tag{3}$$

where U represents the thermal transmittance (W · (m^2 · K)$^{-1}$) for the wall, roof, and window components, A is the surface area (m^2) of each component, T_{out} is the outdoor air temperature and T_{in} is the indoor air temperature.

Solar radiation contributes to the heat load in two ways: a fraction $\alpha_{\mathrm{s}\to\mathrm{a}}$ directly heats the indoor air, while the remainder $(1 - \alpha_{\mathrm{s}\to\mathrm{a}})$ is absorbed by the building's thermal mass and released later, as given in Eq. (4).

$$Q_{\mathrm{solar}}(t) = \alpha_{\mathrm{s}\to\mathrm{a}} \cdot I_{\mathrm{total}}(t) \cdot A_{\mathrm{win}} \cdot \mathrm{SHGC} + Q_{\mathrm{release}}(t) \tag{4}$$

where $Q_{\mathrm{release}}(t)$ denotes the energy released from the thermal mass, depending on the energy stored from previous hours $E_{\mathrm{stored}}(t-1)$ and a release fraction $\beta_{\mathrm{m}\to\mathrm{a}}$, as Eq. (5):

$$Q_{\mathrm{release}}(t) = \frac{E_{\mathrm{stored}}(t-1) \cdot \beta_{\mathrm{m}\to\mathrm{a}}}{\Delta t} \tag{5}$$

The stored energy is updated as Eq. (6):

$$E_{\mathrm{stored}}(t) = E_{\mathrm{stored}}(t-1)(1 - \beta_{\mathrm{m}\to\mathrm{a}}) + (1 - \alpha_{\mathrm{s}\to\mathrm{a}}) \cdot I_{\mathrm{total}}(t) \cdot A_{\mathrm{win}} \cdot \mathrm{SHGC} \cdot \Delta t \tag{6}$$

where $I_{\mathrm{total}}(t)$ is the total solar radiation incident on the windows (W · m^{-2}), SHGC is the solar heat gain coefficient of the windows, A_{win} is the window area (m^2) and Δt is the time step duration (3600 s).

$Q_{\text{vent}}(t)$ is computed as Eq. (7):

$$Q_{\text{vent}}(t) = V_{\text{vent}}(t) \cdot \rho_{\text{air}} \cdot c_{\text{p,air}} \cdot (T_{\text{out}}(t) - T_{\text{in}}(t-1)) \tag{7}$$

where $V_{\text{vent}}(t)$ is the ventilation rate ($\text{m}^3 \cdot \text{s}^{-1}$) varying based on the scheduled number of occupants, ρ_{air} is the density of air ($\text{kg} \cdot \text{m}^{-3}$), and $c_{\text{p,air}}$ is the specific heat capacity of air ($\text{J} \cdot (\text{kg} \cdot \text{K})^{-1}$).

To update the indoor temperature and compute the cooling load (L_{cool}), an intermediate indoor temperature $T'_{\text{in}}(t)$ is determined as Eq. (8):

$$T'_{\text{in}}(t) = T_{\text{in}}(t-1) + \frac{Q_{\text{gain}}(t) \cdot \Delta t}{C_{\text{th}}} \tag{8}$$

where C_{th} is the building's thermal capacity ($\text{J} \cdot \text{K}^{-1}$). If $T'_{\text{in}}(t)$ exceeds the thermostat setpoint T_{set}, SC activates to remove the heat L_{cool} and brings the temperature back to T_{set}. The power of SC is calculated by $P_{\text{SC}}(t) = \frac{L_{\text{cool}}(t)}{\text{COP}}$, where COP denotes the system's coefficient of performance set as 3. The involved parameters of Eqs. (3)–(8) are listed in Supplementary Tables 37–43.

Integration of the mobility and vehicle-to-grid coupled framework

This study integrates the mobility and V2G coupled framework (MOVC)[17] to provide travel-charge profiles of P-PEVs for the subsequent optimization. For the traveling patterns, MOVC uses the Timegeo[47]-based method to simulate the spatial and temporal decisions of users. For the charging patterns, MOVC uses a utility-based model[60] to generate probabilistic choices of charging. This study follows the basic paradigm of MOVC, except that the time interval is set as 1 h and the P-PEV population is set as 1,080,000. The V2G mode considered in this study is V2G when staying (VWS)[17]. The data of all P-PEVs are provided in the CodeOcean repository, including stay duration, stay location and BAU state of charge (SOC) of each vehicle. The transition from user-centric predictions to community-centric scheduling is illustrated in Supplementary Fig. 6.

Community-unit-based optimization formulation

The optimization framework considers the operation of multiple demand-side resources (P-PEVs, BESS, SC DR and RPV) within a CU indexed with *cu*. For the sake of clarity, the index of CU is omitted in Eqs. (9)–(44). P-PEVs and timesteps are indexed with $i \in \mathcal{I}, \mathcal{I} = \{1, \ldots, N_{\text{EV}}\}$ and $t \in \mathcal{T}, \mathcal{T} = \{0, \ldots, T-1\}$, respectively. The objective is to minimize the total economic costs of CUs, as given in Eq. (9):

$$\min\left(\text{Cost}^{\text{V2G}} + \text{Cost}^{\text{BESS}} + \text{Cost}^{\text{SC}} + \text{Cost}^{\text{Penalty}}\right) \tag{9}$$

where $\text{Cost}^{\text{V2G}} = \alpha^{\text{cost}} \cdot C^{\text{V2G}} \cdot \sum_{t \in \mathcal{T}} \sum_{i \in \mathcal{I}^{\text{V2G}}} P^{\text{dis}}_{i,t}$ denotes to the subsidies paid to users for the discharged energy, $\text{Cost}^{\text{BESS}} = C^{\text{BESS}} \cdot Cap^{\text{BESS}} \cdot \frac{r^{\text{BESS}}}{52}$ denotes the equivalent weekly investment cost of BESS, $\text{Cost}^{\text{SC}} = \alpha^{\text{cost}} \cdot C^{\text{SC}} \cdot \sum_{t \in \mathcal{T}} \Delta P^{\text{SC}}_t$ denotes the DR cost of SC, and $\text{Cost}^{\text{Penalty}} = C^{\text{penalty}} \cdot V^{\text{slack}}$ is the virtual penalty term to minimize the possible deviation from the allocated task. α^{cost} is a coefficient corresponding to different subsidy levels, which will be introduced in the following section. C^{V2G} and C^{SC} refer to the unit subsidy costs, set as 0.15 RMB (around 0.021 USD)[17] and 0.043 RMB (around 0.006 USD)[61] per kWh, respectively. Cap^{BESS} is the invested capacity of BESS, C^{BESS} refers to the unit investment cost set as 1200 RMB (around 171.43 USD)[58] per kWh, and r^{BESS} is a coefficient considering annual discount set as 0.13. C^{penalty} is the penalty coefficient set as 100.

This study assumes that all CUs have sufficient bidirectional chargers to support all possible V2G activities. However, the formulation supports the cases where bidirectional chargers are not fully available and the affected vehicles can only perform scheduled charging, as illustrated in Eqs. (10)–(13).

From the P-PEV stay segments of a CU, the hourly stay concurrency is computed as Eq. (10):

$$n^{\text{stay}}_t = \sum_{i \in \mathcal{I}} \mathbf{1}\{t \in \mathcal{T}^{\text{stay}}_i\}, \forall t \in \mathcal{T} \tag{10}$$

The peak stay concurrency in the CU over $\mathcal{T}$ is given as Eq. (11):

$$M^{\text{stay}} = \max_{t \in \mathcal{T}} n^{\text{stay}}_t \tag{11}$$

The peak concurrency is then mapped into the CU-level upper bound of simultaneously available V2G slots, as Eq. (12):

$$N^{\text{V2G}} = \left\lfloor \rho^{\text{infra}} M^{\text{stay}} \right\rfloor \tag{12}$$

where $\rho^{\text{infra}} \in [0, 1]$ is the assumed share of parking positions equipped with bidirectional chargers. Subsequently, stay segments are selected as V2G-eligible by random assignment, while enforcing Eq. (13):

$$\sum_{i \in \mathcal{I}^{\text{V2G}}} \mathbf{1}\{t \in \mathcal{T}^{\text{stay}}_i\} \le N^{\text{V2G}}, \forall t \in \mathcal{T} \tag{13}$$

Equation (13) yields two disjoint sets, namely $\mathcal{I}^{\text{V2G}}$ (V2G-valid segments) and $\mathcal{I}^{\text{sch}}$ (scheduled-charging-only segments). Another set $\mathcal{I}^{\text{dc}}$ denotes the P-PEVs that reject the given subsidy and operate under disordered charging. The three sets satisfy $\mathcal{I} = \mathcal{I}^{\text{V2G}} \cup \mathcal{I}^{\text{sch}} \cup \mathcal{I}^{\text{dc}}$.

The constraints of P-PEVs belonging to the set $\mathcal{I}^{\text{V2G}}$ are given as Eqs. (14)–(22):

if $t \in \mathcal{T}^{\text{stay}}_i$:

$$0 \le P^{\text{ch}}_{i,t} \le \bar{P}_i \tag{14}$$

$$0 \le P^{\text{dis}}_{i,t} \le \bar{P}_i \tag{15}$$

if $t \notin \mathcal{T}^{\text{stay}}_i$:

$$P^{\text{ch}}_{i,t} = 0 \tag{16}$$

$$P^{\text{dis}}_{i,t} = 0 \tag{17}$$

$$\bar{E}_i \cdot \underline{S}_i \le E_{i,t} \le \bar{E}_i \cdot \bar{S}_i \tag{18}$$

$$E_{i,t+1} = E_{i,t} + P^{\text{ch}}_{i,t} \cdot \eta^{\text{EV}} - P^{\text{dis}}_{i,t} / \eta^{\text{EV}} \tag{19}$$

$$E_{i,t^{\text{arr}}} = \bar{E}_i \cdot S_{i,t^{\text{arr}}} \tag{20}$$

$$E_{i,t^{\text{dep}}} \ge E^{\text{need}}_{i,t^{\text{dep}}} \tag{21}$$

$$\sum_{i \in \mathcal{I}} \sum_{t \in \mathcal{T}} P^{\text{ch}}_{i,t} \cdot \eta^{\text{EV}} \ge \sum_{i \in \mathcal{I}} \sum_{t \in \mathcal{T}} P^{\text{dis}}_{i,t} / \eta^{\text{EV}} \tag{22}$$

For P-PEVs belonging to the set $\mathcal{I}^{\text{sch}}$, Eq. (15) turns to $P^{\text{dis}}_{i,t} = 0, i \in \mathcal{I}^{\text{sch}}, t \in \mathcal{T}$. For P-PEVs belonging to the set $\mathcal{I}^{\text{dc}}$, their charging profiles are preprocessed rather than being determined through optimization. The main experiments conducted in this study uses $\rho^{\text{infra}} = 1$, thus $\mathcal{I}^{\text{sch}}$ becomes an empty set.

Following the settings of Li et al.[17], it is assumed that all stays may be scheduled by V2G as shown in Eqs. (14), (15), where $P^{\text{ch}}_{i,t}, P^{\text{dis}}_{i,t}$ refer to the charging and discharging power of P-PEVs and $\bar{P}_i$ is the maximum (dis)charging power. Traveling P-PEVs will not be scheduled as described in Eqs. (16), (17). $E_{i,t}$ refers to the energy of P-PEV i at time t, constrained by Eq. (18), where $\bar{E}_i$ is the maximum capacity and $\underline{S}_i, \bar{S}_i$

represent the lower bound and the upper bound of the state of charge (SOC), respectively. Equation (19) describes the energy transition process of P-PEV i, where the efficiency η^{EV} is set as 0.9. Notably, since $\mathrm{Cost}^{\mathrm{V2G}}$ only applies to $P_{i,t}^{\mathrm{dis}}$, Eq. (19) can be relaxed to a linear format without binary variables[62–64]. Equation (20) denotes the initial SOC $S_{i,t^{\mathrm{arr}}}$ at the arrival time t^{arr}. Equation (21) defines the minimum departure energy as $E_{i,t^{\mathrm{dep}}}^{\mathrm{need}}$, which supports the user to travel either for the next 24 h or to the next charging session[17]. Equation (22) requires a power balance of all P-PEVs ever visiting a specific CU. It ensures that every CU keeps the collective energy of P-PEVs relatively stable, regardless of their activities at other CUs. $\bar{E}_i, \bar{P}_i$ of different P-PEV models are given in Supplementary Table 44[17].

The constraints of SC are given as Eqs. (23)–(25):

$$\underline{P}_t^{\mathrm{SC}} \le P_t^{\mathrm{SC}} \le \bar{P}_t^{\mathrm{SC}} \tag{23}$$

$$\Delta P_t^{\mathrm{SC}} \ge P_t^{\mathrm{SC}} - P_t^{\mathrm{SC,base}} \tag{24}$$

$$\Delta P_t^{\mathrm{SC}} \ge P_t^{\mathrm{SC,base}} - P_t^{\mathrm{SC}} \tag{25}$$

P_t^{SC} is the SC load of a CU aggregated from the buildings within. To ensure thermal comfort of CUs, the SC load is limited between $\underline{P}_t^{\mathrm{SC}}$ and $\bar{P}_t^{\mathrm{SC}}$. The thresholds are determined following Eqs. (2)–(8), setting the setpoint as $T_{\mathrm{set}}+1$ and T_{set}, respectively. The default setpoints T_{set} for different categories of buildings are listed in Supplementary Table 43. Equations (24), (25) give the linearized format of load deviation ΔP_t^{SC}. $P_t^{\mathrm{SC,base}}$ is the base load set identical to $\bar{P}_t^{\mathrm{SC}}$. In winter, P_t^{SC} and $P_t^{\mathrm{SC,base}}$ are set as 0.

The constraints of BESS are given as Eqs. (26)–(31):

$$Cap^{\mathrm{BESS}} \le 50 \cdot N^{\mathrm{bd}} \tag{26}$$

$$P_t^{\mathrm{BESS,ch}} \le \bar{C}_{\mathrm{rate}} \cdot Cap^{\mathrm{BESS}} \cdot z_t^{\mathrm{BESS}} \tag{27}$$

$$P_t^{\mathrm{BESS,dis}} \le \bar{C}_{\mathrm{rate}} \cdot Cap^{\mathrm{BESS}} \cdot (1 - z_t^{\mathrm{BESS}}) \tag{28}$$

$$E_{t+1}^{\mathrm{BESS}} = E_t^{\mathrm{BESS}} + P_t^{\mathrm{BESS,ch}} \cdot \eta^{\mathrm{BESS}} - P_t^{\mathrm{BESS,dis}} / \eta^{\mathrm{BESS}} \tag{29}$$

$$E_0^{\mathrm{BESS}} = E_{T-1}^{\mathrm{BESS}} = 0.5 \cdot Cap^{\mathrm{BESS}} \tag{30}$$

$$E_t^{\mathrm{BESS}} \le Cap^{\mathrm{BESS}} \tag{31}$$

Equation (26) limits the maximum BESS capacity of a building as 50 kWh. Equations (27), (28) define the range of (dis)charging power, where $\bar{C}_{\mathrm{rate}} \cdot Cap^{\mathrm{BESS}}$ refers to the maximum (dis)charging power of BESS correlated to the invested capacity Cap^{BESS} with $\bar{C}_{\mathrm{rate}}$ set as 0.2, and z_t^{BESS} is the binary variable. Equation (29) describes the energy transition process of BESS, with the efficiency η^{BESS} set as 0.953 according to Ref. 59. Equation (30) requires the initial and final energy levels of the BESS remain identical.

The power flows within a CU are defined as Eqs. (32)–(38):

$$P_t^{\mathrm{RPV,EV}} + P_t^{\mathrm{RPV,SC}} + P_t^{\mathrm{RPV,UC}} + P_t^{\mathrm{RPV,Grid}} + P_t^{\mathrm{RPV,BESS}} + P_t^{\mathrm{RPV,curtail}} = P_t^{\mathrm{RPV}} \tag{32}$$

$$P_t^{\mathrm{RPV,SC}} + P_t^{\mathrm{EV,SC}} + P_t^{\mathrm{Grid,SC}} + P_t^{\mathrm{BESS,SC}} = P_t^{\mathrm{SC}} \tag{33}$$

$$P_t^{\mathrm{RPV,UC}} + P_t^{\mathrm{EV,UC}} + P_t^{\mathrm{Grid,UC}} + P_t^{\mathrm{BESS,UC}} = P_t^{\mathrm{UC}} \tag{34}$$

$$P_t^{\mathrm{EV,SC}} + P_t^{\mathrm{EV,UC}} + P_t^{\mathrm{EV,Grid}} + P_t^{\mathrm{EV,BESS}} = \sum_{i \in \mathscr{I}^{\mathrm{V2G}}} P_{i,t}^{\mathrm{dis}} \tag{35}$$

$$P_t^{\mathrm{RPV,EV}} + P_t^{\mathrm{Grid,EV}} + P_t^{\mathrm{BESS,EV}} = \sum_{i \in (\mathscr{I}^{\mathrm{V2G}} \cup \mathscr{I}^{\mathrm{sch}} \cup \mathscr{I}^{\mathrm{dc}})} P_{i,t}^{\mathrm{ch}} \tag{36}$$

$$P_t^{\mathrm{BESS,SC}} + P_t^{\mathrm{BESS,UC}} + P_t^{\mathrm{BESS,EV}} + P_t^{\mathrm{BESS,Grid}} = P_t^{\mathrm{BESS,dis}} \tag{37}$$

$$P_t^{\mathrm{Grid,BESS}} + P_t^{\mathrm{RPV,BESS}} + P_t^{\mathrm{EV,BESS}} = P_t^{\mathrm{BESS,ch}} \tag{38}$$

Equations (32), (33), (34), (35), (36), (37), (38) define the power flows of RPV, SC, uncontrollable devices (UC), P-PEVs and BESS, respectively.

The constraints of grid interaction are given as Eqs. (39)–(43):

$$P_t^{\mathrm{buy}} = P_t^{\mathrm{Grid,EV}} + P_t^{\mathrm{Grid,SC}} + P_t^{\mathrm{Grid,UC}} + P_t^{\mathrm{Grid,BESS}} \tag{39}$$

$$P_t^{\mathrm{sell}} = P_t^{\mathrm{EV,Grid}} + P_t^{\mathrm{RPV,Grid}} + P_t^{\mathrm{BESS,Grid}} \tag{40}$$

$$P_t^{\mathrm{buy}} - P_t^{\mathrm{sell}} \ge -\bar{P}^{\mathrm{peak}} \tag{41}$$

$$(P_t^{\mathrm{buy}} - P_t^{\mathrm{sell}}) - (\delta_t^+ - \delta_t^-) = P_t^{\mathrm{target}} \tag{42}$$

$$\sum_{t \in \mathcal{T}} \delta_t^+ \le V^{\mathrm{slack}} \tag{43}$$

Equations (39), (40) define the imported load and the exported load of a CU, respectively. Equation (41) requires that the maximum feed-in power of a CU should not exceed its BAU load peak[16]. Equation (42) describes the deviation between the net load $P_t^{\mathrm{buy}} - P_t^{\mathrm{sell}}$ and the allocated task P_t^{target}, where δ_t^+, δ_t^- denote the upward and downward deviation, respectively. δ_t^+ represents the AOS generated when the net load exceeds P_t^{target}, and δ_t^- represents the AOC generated conversely. Since AOS is related to the carbon emission, this study uses Eq. (43) to link δ_t^+ with the term $\mathrm{Cost}^{\mathrm{Penalty}}$ in Eq. (9). All decision variables are non-negative. P_t^{target} is the allocated generation-demand mismatch for a single CU indexed with cu, given as Eq. (44):

$$P_t^{\mathrm{target}} = \lambda_{cu} \cdot \left(P_t^{\mathrm{Gen}} - P_t^{\mathrm{Cons}} + \sum_{bd} P_t^{bd} \right) \tag{44}$$

where P_t^{Gen} and P_t^{Cons} are the generation and consumption load of the city, and $\sum_{bd} P_t^{bd}$ is the aggregated load of all considered buildings in the city. Two allocation methods are designed to determine λ_{cu}, namely FQA and PBA, which will be introduced in the following sections. More details about computing the city-level generation-demand mismatch are given in Supplementary Note 7.

FQA is designed to simulate a unified policy, allocating tasks for each CU according to its weighted proportion of flexibility resources (P-PEVs and BESS). λ_{cu} is given as Eq. (45):

$$\lambda_{cu} = \lambda_{\mathrm{BESS}} \cdot \frac{N_{\mathrm{bd},cu}}{\sum_{cu} N_{\mathrm{bd},cu}} + \lambda_{EV} \cdot \frac{Visit_{\mathrm{EV},cu}}{\sum_{cu} Visit_{\mathrm{EV},cu}} \tag{45}$$

where $N_{\mathrm{bd},cu}$ is the number of buildings in cu, and $Visit_{\mathrm{EV},cu}$ is the number of P-PEV visits of cu. According to Eq. (26), $N_{\mathrm{bd},cu}$ is proportional to the maximum BESS capacity of cu. As shown in Fig. 3, five FQA plans are compared, setting $(\lambda_{\mathrm{EV}}, \lambda_{\mathrm{BESS}}) = (0,1), (0.3,0.7), (0.5,0.5), (0.7,0.3), (1,0)$, respectively.

PBA is designed to further uncover the potential of CUs which have abundant flexibility resources, since the unified tasks given by FQA may limit these CUs to operate all-out. An upper bound $\bar{\lambda}_{cu}$ is calculated such that the corresponding $\bar{P}^{\mathrm{target},cu}$ given by Eq. (44) yields identical upward and downward deviation compared with the BAU building load $\sum_{bd} P^{bd,cu}$. Due to the load shifting nature of flexibility resources, $\bar{P}^{\mathrm{target},cu}$ is appropriate for cu assuming that cu has

sufficient resources. In practice, $\sum_{cu}\bar{\lambda}_{cu}$ is larger than 1. The lower bound is thus set as $\underline{\lambda}_{cu}=\bar{\lambda}_{cu}$*0.05. Each cu will operate multiple times k with uniformly sampled weight $\lambda_{cu,k}\in[\underline{\lambda}_{cu},\bar{\lambda}_{cu}]$ to obtain a collection of choices $\{\mathscr{K}_{cu}\}=\{(\lambda_{cu,k},V_{cu,k}^{\text{slack}})\}$. This study utilizes dynamic programming (DP) to derive an optimal decision such that $\sum_{cu}\lambda_{cu,k}^{*}=1$ and $\sum_{cu}V_{cu,k}^{*\text{slack}}$ reaches a minimum. It is assumed that all CUs must be selected. Considering the computational costs, this study sets $k\le 20$ and the minimum step length of DP as 10^{-5}. Details of the DP process are introduced in Supplementary Note 8.

User participation mechanism

It is assumed that a single P-PEV user (or a building) requires a specific subsidy to participate in V2G (or SC DR). The subsidy costs follow the normal distribution[17,33] as given in Eq. (46):

$$\xi^{i}\sim N(\mu_c,\delta_c) \tag{46}$$

Policy makers determine the subsidy level γ_{Sub} to adjust the scale of participation. A user (or building) indexed with i will accept to be scheduled if Eq. (47)

$$\xi^{i}\le\gamma_{\text{Sub}}\cdot\mu_c \tag{47}$$

This study sets $\mu_c^{\text{V2G}},\delta_c^{\text{V2G}}=0.15$, 0.075 RMB (around 0.02, 0.01 USD) per kWh, and sets $\mu_c^{\text{SC}},\delta_c^{\text{SC}}=0.022$, 0.011 RMB (around 0.003, 0.001 USD) per kWh. Subsidy level Sub = 1, 2, 3, 4 corresponds to $\gamma_{\text{Sub}}=0.5,1,1.5,2.\alpha^{\text{cost}}$ for calculating Cost^{V2G}, Cost^{SC} in Eq. (9) is equal to $\gamma_{\text{Sub}}\cdot\mu_c$. For results given in Figs. 3, 4, 6, this study sets $\gamma_{\text{Sub}}=2$.

Carbon emission estimation

In this study, it is assumed that AOS is supplied by 70% of local gas power and 30% of external power transmission. Referring to the study of Jia et al.[65], the carbon emission factors of the former under ZC30, ZC50, ZC80 are set as 0.380, 0.367, 0.363 kg CO_2 per kWh, and the values of the latter are 0.338, 0.277, 0.200 kg CO_2 per kWh.

Summary of model assumptions

This study assumes that all CUs participate in DSRM. Under ZC30, ZC50 and ZC80, the respective shares of nuclear, PV and wind power are assumed to be 10%, 10% and 10%; 18%, 22% and 10%; and 33%, 37% and 10%. AOS is assumed to be supplied through gas power or external power transmission, accounting for 70% and 30% of the shortage, respectively. The general mobility patterns of P-PEVs are assumed to remain consistent across seasons. The proportions of available RPV area deployed with PV panels are assumed to be 30%, 50% and 80% under the three corresponding zero-carbon penetration scenarios. For each building, the SC load is determined by its thermal dynamics, primarily indoor air temperature. Participation in V2G operation or SC DR is assumed to require a user- or building-specific subsidy. For participating P-PEVs, all stay segments are assumed to be available for V2G scheduling, and each CU is assumed to have sufficient bidirectional charging infrastructure to support all possible V2G activities.

Data requirements, computational burden, and transferability

From coarse to fine in terms of data granularity, the framework requires city-level load profiles, solar radiation, temperature, geographic outlines of CUs, building energy consumption, deployable rooftop PV areas, and P-PEV stay segments (arrival/departure times and arrival stage of charge). Detailed dataset descriptions are provided in subsection Datasets in Methods. For computational reference, on a PC with an Intel i9-14900K CPU and 128 GB RAM using the Gurobi solver with 8 parallel processes under subsidy level 4, solving an FQA instance takes 3–4 h, while a PBA instance requires approximately 14 h.

For cities lacking granular data, simplified methods ensure transferability. CU boundaries can be determined via public street outlines and road networks. Building energy use can be estimated through typical community archetypes instead of individual simulations. RPV areas can be estimated via kilometer-level grid-based extraction with assumed deployment ratios. If individual P-PEV trajectories are unavailable, localized traffic densities can be estimated, with arrival/departure times and arrival state of charge modeled using probabilistic distributions aligned with community functionalities (residential, commercial, office).

Reporting summary

Further information on research design is available in the Nature Portfolio Reporting Summary linked to this article.

Data availability

The data generated in this study have been deposited at the CodeOcean repository here[66]. Source data for reproducing the figures are available at Figshare repository here[67]. Source data are provided as a Source Data file. Source data are provided with this paper.

Code availability

The Python scripts developed for data analysis have been deposited at the CodeOcean repository here[66].

References

1. National Development and Reform Commission (NDRC) & National Energy Administration (NEA). *Guidelines on Promoting the Integration and Regulation of Renewable Energy* (2025).
2. Central Committee of the Communist Party of China & China State Council. *Working Guidance for Carbon Peaking and Carbon Neutrality in Full Implementation* (Beijing, 2021).
3. Zheng, D. et al. Strategies for climate-resilient global wind and solar power systems. *Nature* **643**, 1263–1270 (2025).
4. Riepin, I., Brown, T. & Zavala, V. M. Spatio-temporal load shifting for truly clean computing. *Adv. Appl. Energy* **17**, 100202 (2025).
5. Li, J., Ho, M. S., Xie, C. & Stern, N. China's flexibility challenge in achieving carbon neutrality by 2060. *Renew. Sustain. Energy Rev.* **158**, 112112 (2022).
6. Nilges, B., Reinert, C. & von der Assen, N. Is demand-side management environmentally beneficial? Analyzing the greenhouse gas emissions due to load shifting in electric power systems. *J. Clean. Prod.* **434**, 140062 (2024).
7. International Energy Agency (IEA). *Energy Efficiency 2021* (Paris, 2021).
8. National Energy Administration (NEA). *Guiding Opinions of the National Energy Administration on Supporting Innovation and Development of New Business Entities in the Power Sector*. NEA Document [2024] No. 93 (National Energy Administration, Beijing, 2024).
9. Jiang, H. et al. Globally interconnected solar-wind system addresses future electricity demands. *Nat. Commun.* **16**, 4523 (2025).
10. Wessel, J. et al. Regional coordination can alleviate the cost burden of a low-carbon electricity system. *Nat. Commun.* **16**, 9033 (2025).
11. Zhuo, Z. et al. Cost increase in the electricity supply to achieve carbon neutrality in China. *Nat. Commun.* **13**, 3172 (2022).
12. Peng, L., Mauzerall, D. L., Zhong, Y. D. & He, G. Heterogeneous effects of battery storage deployment strategies on decarbonization of provincial power systems in China. *Nat. Commun.* **14**, 4858 (2023).
13. Sun, T. et al. Solar and battery can reduce energy costs and provide affordable outage backup for US households. *Nat. Energy* **10**, 1025–1040 (2025).
14. Li, J. et al. Redesigning electrification of China's ammonia and methanol industry to balance decarbonization with power system security. *Nat. Energy* **10**, 762–773 (2025).

15. Yang, R. et al. Urban rooftops for food and energy in China. *Nat. Cities* **1**, 741–750 (2024).
16. Shi, M., Lu, X. & Craig, M. T. Unveiling deployable rooftop solar potential across Chinese cities. *Nat. Cities* **2**, 650–661 (2025).
17. Li, K. et al. Unlocking vehicle-to-grid potential of load shifting in China's megacities considering comprehensive real-world behaviors. *Nat. Commun.* **16**, 10087 (2025).
18. Kazemian, A. & Xiang, C. Large-scale analysis of photovoltaic, photovoltaic-thermal, and solar thermal systems in high-density urban environments. *Appl. Energy* **401**, 126765 (2025).
19. Qi, T., Hui, H., Feng, W. & Song, Y. Flexible resource endowment of urban buildings considering climate diversity in China. *Carbon Neutrality* **4**, 1–19 (2025).
20. Ping, D. et al. City-scale information modelling for urban energy resilience with optimal battery energy storages in Hong Kong. *Appl. Energy* **378**, 124813 (2025).
21. Yap, W., Wu, A. N., Miller, C. & Biljecki, F. Revealing building operating carbon dynamics for multiple cities. *Nat. Sustain.* **8**, 1199–1210 (2025).
22. Chen, Y. et al. A building-scale modeling framework for urban net-zero transitions in Nanjing. *Nat. Commun.* **16**, 8954 (2025).
23. Vahid-Ghavidel, M. et al. Integrated energy demand-supply modeling for low-carbon neighborhood planning. *Appl. Energy* **358**, 122560 (2024).
24. Yang, T., Wang, Q., Wang, X., Wang, L. & Geng, Y. Low-carbon economic distributed dispatch for district-level integrated energy system considering privacy protection and demand response. *Appl. Energy* **383**, 125389 (2025).
25. Liao, W., Xiao, F., Li, Y. & Peng, J. Comparative study on electricity transactions between multi-microgrid: a hybrid game theory-based peer-to-peer trading in heterogeneous building communities considering electric vehicles. *Appl. Energy* **367**, 123459 (2024).
26. Wei, T. et al. City-scale roof-top photovoltaic deployment planning. *Appl. Energy* **368**, 123461 (2024).
27. Ji, N., Zhu, R., Huang, Z. & You, L. An urban-scale spatiotemporal optimization of rooftop photovoltaic charging of electric vehicles. *Urban Inform.* **3**, 4 (2024).
28. Cliff, A. D. & Ord, J. K. *Spatial Processes: Models & Applications* (Pion, 1981).
29. Shi, M. et al. Opportunity of rooftop solar photovoltaic as a cost-effective and environment-friendly power source in megacities. *Iscience* **25**, 104890 (2022).
30. Zhou, J. et al. Decentralized electric vehicle charging enables large-scale photovoltaic integration in tropical cities. *Nat. Commun.* **17**, 3037 (2026).
31. Sunter, D. A., Castellanos, S. & Kammen, D. M. Disparities in rooftop photovoltaics deployment in the United States by race and ethnicity. *Nat. Sustain.* **2**, 71–76 (2019).
32. Carley, S. & Konisky, D. M. The justice and equity implications of the clean energy transition. *Nat. Energy* **5**, 569–577 (2020).
33. Wang, X., Nie, Y. & Cheng, K.-W. E. Distribution system planning considering stochastic EV penetration and V2G behavior. *IEEE Trans. Intell. Transpor. Syst.* **21**, 149–158 (2019).
34. Lee, W., Woo, J., Kim, Y. -g & Koo, Y. Vehicle-to-grid as a competitive alternative to energy storage in a renewable-dominant power system: an integrated approach considering both electric vehicle drivers' willingness and effectiveness. *Energy* **310**, 133194 (2024).
35. Xu, L., Lei, S., Hu, M., Srinivasan, D. & Song, Z. Proactive grid investment enables V2G for 100% adoption of electric vehicles in urban areas. *Joule* **10**, 102393 (2026).
36. Xu, Y., Çolak, S., Kara, E. C., Moura, S. J. & González, M. C. Planning for electric vehicle needs by coupling charging profiles with urban mobility. *Nat. Energy* **3**, 484–493 (2018).
37. Wu, J., Powell, S., Xu, Y., Rajagopal, R. & Gonzalez, M. C. Planning charging stations for 2050 to support flexible electric vehicle demand considering individual mobility patterns. *Cell Rep. Sustain.* **1**, 100006 (2024).
38. Yamaguchi, Y. et al. Large-scale spatiotemporal modeling of travel behavior, electric vehicle charging demand, and flexibility based on human mobility big data. *Energy* **335**, 137804 (2025).
39. Mousa, H. H., Mahmoud, K. & Lehtonen, M. Recent developments of demand-side management towards flexible DER-rich power systems: a systematic review. *IET Gener., Transm. Distrib.* **18**, 2259–2300 (2024).
40. Mousa, H. H., Mahmoud, K. & Lehtonen, M. Multi-timescale coordinated planning of BESS, seasonal hydrogen storage, and dynamic DR for unbalanced RES-rich microgrids. *Energy Convers. Manag.* **346**, 120510 (2025).
41. Orfanoudakis, S. et al. Ev2gym: a flexible v2g simulator for EV smart charging research and benchmarking. *IEEE Trans. Intelligent Transport. Syst.* **26**, 2410–2421 (2024).
42. Xu, L., Lin, N., Poor, H. V., Xi, D. & Perera, A. T. D. Quantifying cascading power outages during climate extremes considering renewable energy integration. *Nat. Commun.* **16**, 2582 (2025).
43. AutoNavi. *Amap*, https://www.amap.com/ (2025).
44. Zhu, Y., Zhang, Y., Zhang, Y. & Zheng, B. Tracing CO2 emissions across megacity landscapes: beyond citywide totals to structural heterogeneity and mitigation. *Environ. Sci. Ecotechnol.* **27**, 100602 (2025).
45. Lawrie, L. K. & Drury B. Crawley. *Development of Global Typical Meteorological Years (TMYx) (paper in progress)*, https://climate.onebuilding.org (2022).
46. Shenzhen Municipal Bureau of Planning and Natural Resources. *Shenzhen Municipal Bureau of Planning and Natural Resources* https://pnr.sz.gov.cn (2025).
47. Jiang, S. et al. The TimeGeo modeling framework for urban mobility without travel surveys. *Proc. Natl. Acad. Sci. USA* **113**, E5370–E5378 (2016).
48. Lanmei Energy Research Center. *Guangdong-Hong Kong-Macao Greater Bay Area Power Development Report* (China Electric Power Press, 2021).
49. Southern Power Grid Energy Development Research Institute. *Greater Bay Area Power Development Report* (China Electric Power Press, 2022).
50. Staffell, I. & Pfenninger, S. Using bias-corrected reanalysis to simulate current and future wind power output. *Energy* **114**, 1224–1239 (2016).
51. Shenzhen Housing and Construction Bureau. *Design Standard for Energy Efficiency of Public Buildings: SJG 44-2025* (Shenzhen Housing and Construction Bureau, Shenzhen, 2025).
52. Shenzhen Housing and Construction Bureau. *Design Standard for Energy Efficiency of Residential Buildings: SJG 45-2025* (Shenzhen Housing and Construction Bureau, Shenzhen, 2025).
53. Qi, F. & Wang, Y. A new calculation method for shape coefficient of residential building using Google Earth. *Energy Build.* **76**, 72–80 (2014).
54. Google. *Google Earth*, https://earth.google.com/web (2025).
55. ASHRAE. *ASHRAE*, https://www.ashrae.org/ (2025).
56. Ladybug Tools LLC. *Ladybug Tools*, https://www.ladybug.tools/ (2025).
57. U.S. Department of Energy. *EnergyPlus* https://energyplus.net/ (2025).
58. Zhang, Y., Han, X., Wei, T., Zhao, X. & Zhang, Y. Techno-environmental-economical performance of allocating multiple energy storage resources for multi-scale and multi-type urban forms towards low carbon district. *Sustain. Cities Soc.* **99**, 104974 (2023).
59. Chen, S. X., Gooi, H. B. & Wang, M. Q. Sizing of energy storage for microgrids. *IEEE Trans. Smart Grid* **3**, 142–151 (2011).

60. Liu, Y. S., Tayarani, M. & Gao, H. O. An activity-based travel and charging behavior model for simulating battery electric vehicle charging demand. *Energy* **258**, 124938 (2022).
61. Astriani, Y., Shafiullah, G. & Shahnia, F. Incentive determination of a demand response program for microgrids. *Appl. Energy* **292**, 116624 (2021).
62. Yang, P. & Nehorai, A. Joint optimization of hybrid energy storage and generation capacity with renewable energy. *IEEE Trans. Smart Grid* **5**, 1566–1574 (2014).
63. Li, Q. & Vittal, V. Non-iterative enhanced SDP relaxations for optimal scheduling of distributed energy storage in distribution systems. *IEEE Trans. Power Syst.* **32**, 1721–1732 (2016).
64. Yang, S., Gao, H. O. & You, F. Integrated optimization in operations control and systems design for carbon emission reduction in building electrification with distributed energy resources. *Adv. Appl. Energy* **12**, 100144 (2023).
65. Jia, M. et al. Optimization of electricity generation and assessment of provincial grid emission factors from 2020 to 2060 in China. *Appl. Energy* **373**, 123838 (2024).
66. Li, K. Code instruction for Facilitating megacity electricity decarbonization via grid-interactive demand-side resource management. CodeOcean. https://doi.org/10.24433/CO.6637726.v1 (2026).
67. Li, K. Source data for Facilitating megacity electricity decarbonization via grid-interactive demand-side resource management. figshare. *Dataset* https://doi.org/10.6084/m9.figshare.31046854 (2026).
68. Anselin, L. Local indicators of spatial association—LISA. *Geogr. Anal.* **27**, 93–115 (1995).

Author contributions

K.L. developed the methodology and software, performed the validation and formal analyses, curated the data, prepared the visualizations, wrote the original draft, and revised the manuscript. S.T. developed the methodology and software, performed the validation, prepared the visualizations, wrote the original draft and revised the manuscript. Z.X. contributed to the methodology and software, and revised the manuscript. R.R. prepared the visualizations. Y.H.Z. curated the data. R.M. contributed to software development. H.Q., B.L., J.K., and Y.J. contributed to the conceptualization and administration of the project. Y.Z. conceived and supervised the study, provided resources, administered the project, acquired funding, and contributed to writing the original draft and revising the manuscript. K.L., S.T., Z.X., R.R., Y.H.Z., R.M., H.Q., B.L., J.K., Y.J., and Y.J. contributed to reviewing and editing the manuscript.

Funding

Y.Z. and H.Q. were supported by Shenzhen Science and Technology Program (Grant No. KCXST20221021111608020) and China Construction Key Research Program (Grant No. CSCEC–2024-Z-22).

Competing interests

The authors declare no competing interests.

Additional information

Supplementary information The online version contains supplementary material available at https://doi.org/10.1038/s41467-026-76799-4.

Correspondence and requests for materials should be addressed to Yi Zhang.

Peer review information *Nature Communications* thanks reviewers Hossam H. H. Mousa and Daniel Horak for their contribution to the peer review of this work. A peer review file is available.

Reprints and permissions information is available at http://www.nature.com/reprints

Publisher's note Springer Nature remains neutral with regard to jurisdictional claims in published maps and institutional affiliations.

Open Access This article is licensed under a Creative Commons Attribution-NonCommercial-NoDerivatives 4.0 International License, which permits any non-commercial use, sharing, distribution and reproduction in any medium or format, as long as you give appropriate credit to the original author(s) and the source, provide a link to the Creative Commons licence, and indicate if you modified the licensed material. You do not have permission under this licence to share adapted material derived from this article or parts of it. The images or other third party material in this article are included in the article's Creative Commons licence, unless indicated otherwise in a credit line to the material. If material is not included in the article's Creative Commons licence and your intended use is not permitted by statutory regulation or exceeds the permitted use, you will need to obtain permission directly from the copyright holder. To view a copy of this licence, visit http://creativecommons.org/licenses/by-nc-nd/4.0/.

© The Author(s) 2026